From small scale variability to mesoscale stability in surface ocean pH: implications for air-sea CO₂ equilibration

Louise Delaigue[1,2], Gert-Jan Reichart[1,3], Li Qiu[4], Eric P. Achterberg[4], Yasmina Ourradi[1], Chris Galley[5,6], André Mutzberg[4] and Matthew P. Humphreys[1]

[1]Department of Ocean Systems (OCS), NIOZ Royal Netherlands Institute for Sea Research, PO Box 59, 1790 AB Den Burg (Texel), the Netherlands
[2]Sorbonne Université, CNRS, Laboratoire d'Océanographie de Villefranche, LOV, 06230 Villefranche-sur-Mer, France
[3]Department of Earth Sciences, Utrecht University, 3584 CS Utrecht, The Netherlands
[4]GEOMAR Helmholtz Centre for Ocean Research, Kiel, Germany
[5]Department of Earth Sciences, Memorial University of Newfoundland, St. John's, NL, A1B 3X5, Canada
[6]Department of Earth and Environmental Sciences, University of Ottawa, Ottawa, ON, K1N 6N5, Canada

Correspondence to: Louise Delaigue (louise.delaigue@imev-mer.fr)

Abstract. One important aspect of understanding ocean acidification is the nature and drivers of pH variability in surface waters on smaller spatial (i.e., areas up to 100 km²) and temporal (i.e., days) scales. However, there has been a lack of high-quality pH data at sufficiently high resolution. Here, we describe a simple optical system for continuous high-resolution surface seawater pH measurements. The system includes a PyroScience pH optode placed in a flow-through cell directly connected to the underway supply of a ship through which near-surface seawater is constantly pumped. Seawater pH is measured at a rate of 2 to 4 measurements min⁻¹ and is cross-calibrated using discrete carbonate system observations (total alkalinity, dissolved inorganic carbon, and nutrients). This setup was used during two research cruises in different oceanographic conditions: the North Atlantic Ocean (December 2020-January 2021) and the South Pacific Ocean (February-April 2022). By leveraging this novel high-frequency measurement approach, our findings reveal fine-scale fluctuations in surface seawater pH across the North Atlantic and South Pacific Oceans. While temperature is a significant abiotic factor driving these variations, it does not account for all observed changes. Instead, our results highlight the interplay between temperature, biological activity, and waters with distinct temperature-salinity properties on pH. Notably, the variability differed between the two regions, suggesting differences in the dominant factors influencing pH. In the South Pacific, biological processes appeared to be mostly responsible for pH variability, while in the North Atlantic, additional abiotic and biotic factors complicated the correlation between expected and observed pH changes. While our findings indicate that broader ocean-basin scale analyses based on lower-resolution datasets can effectively capture surface ocean CO₂ variability at a global scale, they also highlight the necessity of fine-scale observations for resolving regional processes and their drivers, which is essential for improving predictive models of ocean acidification and air-sea CO₂ exchange.

1 Introduction

Ocean chemistry is changing due to the uptake of anthropogenic CO₂ from the atmosphere (DeVries, 2022). The uptake of atmospheric CO₂ by the ocean's surface increases hydrogen ion concentration, a process known as ocean acidification, which has led to a 30–40% rise in hydrogen ion concentration (i.e. surface seawater acidity) and a corresponding pH decrease of ~0.1 since around 1850 (Gattuso et al., 2015; Jiang et al., 2019; Orr et al., 2005). These changes have already significantly impacted marine organisms, especially marine calcifiers (Doney et al., 2020; Gattuso et al., 2015; Osborne et al., 2020), and pH is projected to decline by ~0.3 by 2100 (Figuerola et al., 2021).

High-resolution studies of surface ocean carbonate chemistry and air-sea CO₂ exchange have significantly advanced our understanding of the upper ocean's carbon cycle. However, gaps

46 remain, particularly at fine spatio-temporal scales (e.g., variability over hours and a few
47 kilometers). At these scales, changes in pH over short time periods can be an important control
48 on the ocean's buffering capacity and response to CO_2 uptake, highlighting the need for further
49 detailed observations (Cornwall et al., 2013; Egilsdottir et al., 2013; James et al., 2020; Qu et al.,
50 2017; Wei et al., 2022).

52 Advancements in the last decade and a half have enhanced the capacity for accurate and precise
53 in-situ pH measurements. For example, Martz et al. (2010) developed an autonomous sensor
54 tailored for continuous deployment in marine environments that allows recording of high-
55 resolution pH fluctuations. Autonomous surface vehicles in coastal upwelling systems have also
56 been used to capture intricate partial pressure of CO_2 (pCO_2) and pH dynamics, even in complex
57 environments where rapid biogeochemical changes occur due to natural phenomena like
58 upwelling (Chavez et al., 2018; Cryer et al., 2020; Possenti et al., 2021). Staudinger et al. (2018)
59 also developed an optode system capable of simultaneously measuring oxygen, carbon dioxide,
60 and pH in seawater. This system was designed for extended deployment (i.e. days) in marine
61 environments, enabling continuous monitoring (with measurement intervals between 1 second
62 and 1 hour) of these parameters. Additionally, Sutton et al. (2019) detailed the implementation of
63 autonomous seawater pCO_2 and pH time series from 40 surface buoys, broadening the scope of
64 observations at fixed time series sites. Staudinger et al. (2019) introduced fast and stable optical
65 pH sensor materials specifically for oceanographic applications, enhancing the ability to measure
66 pH under various environmental conditions.

68 These technological advancements have facilitated significant scientific progress. Field
69 measurements conducted using submersible spectrophotometric sensors have revealed fine-scale
70 variations in pH in coastal waters and shed light on localized acidification processes (Cornwall et
71 al., 2013). The implementation of autonomous seawater pCO_2 and pH time series as described by
72 Sutton et al. (2019) has enhanced our ability to characterize sub-seasonal variability in the ocean.
73 These efforts represent important progress that can be built upon to further understand fine-scale
74 ocean dynamics.

76 Fine spatio-temporal scale variability in surface ocean pH is hard to capture because it is driven
77 by a complex interplay of processes, including physical mixing, biological activity (i.e.
78 photosynthesis and respiration), thermal variability, and air-sea CO_2 fluxes (Faassen et al., 2023;
79 Hofmann et al., 2011; Price et al., 2012). Physical mixing moderates surface oceanic pH by
80 redistributing dissolved CO_2, nutrients, and heat throughout the water column. Mixing also
81 mitigates extreme pH fluctuations by diluting surface concentrations of CO_2 during periods of
82 high biological activity or temperature-induced CO_2 release (Egea et al., 2018; Li et al., 2019).
83 Photosynthetic activity can decrease CO_2, leading to an increase in pH during daylight hours,
84 while respiration dominates at night, releasing CO_2 and lowering pH (Fujii et al., 2021; Jokiel et
85 al., 2014). Warmer waters decrease CO_2 solubility and increase pH, while cooler waters increase
86 solubility, promoting CO_2 uptake and decreasing pH, although the timescale of these processes
87 differs, with some changes occurring instantaneously and others after equilibration (Zeebe &
88 Wolf-Gladrow, 2001). Instantaneous changes are driven by physical and chemical reactions,
89 while equilibration processes involve longer-term adjustments such as air-sea gas exchange and
90 the mixing of surface waters with deeper layers (Emerson & Hedges, 2008). When atmospheric
91 CO_2 exceeds oceanic CO_2, the ocean takes up CO_2, lowering pH; conversely, when atmospheric

92   CO_2 decreases below oceanic CO_2, outgassing occurs, raising pH (Caldeira & Wickett, 2005; Orr
93   et al., 2005). Although each of these processes has its distinct impact on pH, their combined
94   effects regulate the ocean's carbon cycle and its interaction with the atmosphere.

96   Recent studies on air-sea CO_2 equilibration timescales have highlighted significant regional
97   variations, particularly between the North Atlantic and South Pacific Oceans (Jones et al., 2014).
98   In the North Atlantic, equilibration timescales for CO_2 between the atmosphere and the ocean's
99   surface mixed layer vary significantly with latitude. In regions above 55°N, these timescales can
100 extend up to 18 months, while at lower latitudes, such as around 30°N, they range from 3 to 6
101 months (Jones et al., 2014). These long equilibration timescales reduce the extent to which the
102 ocean can buffer short-term changes in surface pH. On pentadal and longer timescales, the air-
103 sea CO_2 flux in the North Atlantic is driven primarily by changes in ΔpCO_2, while gas transfer
104 velocity plays a more significant role only on interannual and shorter timescales (Couldrey et al.,
105 2016).

107 Cooler temperatures at higher latitudes increase CO_2 solubility, resulting in higher dissolved
108 inorganic carbon (DIC), and upwelling brings DIC and total alkalinity (TA)-rich deep waters to
109 the surface (Wu et al., 2019). These factors further increase the amount of CO_2 that needs to
110 exchange with the atmosphere, further prolonging equilibration times. The South Pacific, with its
111 shallower mixed layers and higher average surface temperatures, facilitates shorter equilibration
112 times and enhances CO_2 uptake rates (i.e. 3 to 4 months; Jones et al., 2014). Wu et al. (2019)
113 also showed that high biological productivity in these areas significantly impacts DIC,
114 potentially reducing surface DIC more quickly.

116 Here, we test a high-frequency optical system to investigate how surface seawater pH varies
117 across fine spatio-temporal scales, focusing on changes occurring over areas up to 100 km^2 and
118 timescales of hours to days across different ocean basins (i.e., North Atlantic and South Pacific
119 Oceans) and identify abiotic and biotic factors driving these variations. We use direct, high-
120 frequency measurements of surface seawater pH and estimate TA to resolve the rest of the
121 carbonate system. This novel setup provides new insights into processes, such as temperature,
122 hydrodynamic mixing and biological activity, influence fine-scale spatio-temporal variability in
123 pH.

2 Materials and Procedures

2.1 Study areas
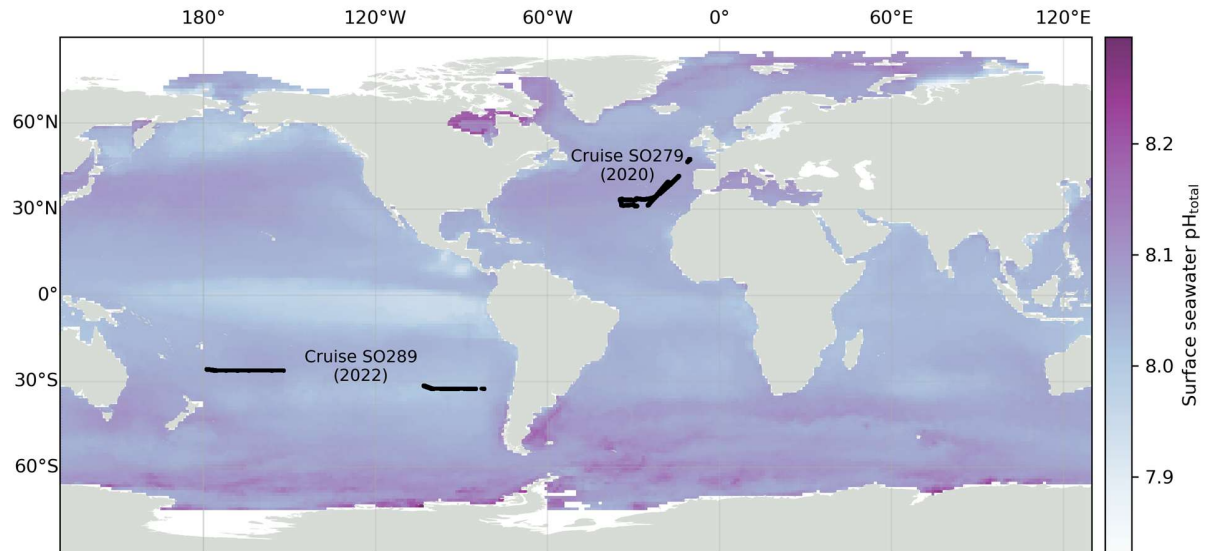
Figure 1. Locations of pH measurements during two oceanographic cruises used in this study: SO279 in the North Atlantic (December 2020 to January 2021) and SO289 in the South Pacific (February-April 2022). Surface seawater pH on the total scale for December 2022 from the OceanSODA product is shown in the background (Gregor & Gruber, 2020).

Two datasets from separate oceanic regions were used: research expeditions SO279 in the North Atlantic Ocean and SO289 in the South Pacific Ocean, both on the German R/V Sonne (Fig. 1).

Expedition SO279 in January to December 2020, conducted in the Azores Region of the North Atlantic Ocean (Fig. 1), was part of the NAPTRAM research program investigating the transport pathways of plastic and microplastic debris (Beck et al., 2021). The data collection included discrete samples from the CTD rosette (n=77; (Delaigue et al., 2021a), with measurements of DIC, TA and nutrients (silicate, phosphate ammonium, nitrite, and nitrate + nitrite); discrete samples from the underway water system (UWS; n=51; (Delaigue et al., 2021b) also measuring these parameters; and a high-resolution UWS timeseries of ocean surface pH (over 43,000 datapoints; (Delaigue et al., 2021c).

The South Pacific GEOTRACES Cruise SO289, from Valparaiso (Chile) to Noumea (New Caledonia) under the GEOTRACES GP21 initiative, was conducted from February to April 2022 (Fig. 1; (Achterberg et al., 2022). The data collection also included the same parameters as SO279, with discrete samples from the CTD rosette (n=395; (Delaigue, Ourradi, Ossebar, et al., 2023), discrete samples from the UWS (n=32; (Delaigue, Ourradi, et al., 2023a) and another high-resolution UWS timeseries of ocean surface pH from the optode system (over 78,000 datapoints; (Delaigue, Ourradi, et al., 2023b).

2.2 Integrated shipboard optode system for continuous pH measurements

We used a pH optode (PHROBSC-PK8T, for pH range 7.0 – 9.0 on the total scale; PyroScience GmbH), made of a robust cap adapter fiber with a stainless-steel tip (length=10cm,

154 diameter=4mm) and disposable plastic screw cap with an integrated pH sensor. The total scale
155 accounts for sulfate ion dissociation in seawater, providing a more accurate representation of
156 carbonate system equilibria compared to other pH scales commonly used in marine chemistry.
157 Unless explicitly stated otherwise, all references to pH in this manuscript refer to pH on the total
158 scale. The manufacturer-reported accuracy of the optode is ±0.05 for pH 7.5–9.0 and ±0.1 for pH
159 7.0–7.5 after a two-point calibration, with a precision of ±0.003 at pH 8.0.
160
161 The optode was connected to a meter combined with a pressure-stable optical connector (optical
162 feed-through; OEM module Pico-pH-SUB; PyroScience GmbH; Fig. 2). Briefly, the optical pH
163 sensor is constructed using the PyroScience REDFLASH technology, which uses a pH neutral
164 reference indicator and a pH responsive luminescent dye. These elements are activated using a
165 specifically tuned orange-red light with a wavelength ranging between 610-630 nm, which
166 triggers a bright luminescence emission in the near-infrared (NIR) band, spanning from 760-790
167 nm. At elevated pH, the fluorescence from the pH marker is diminished, leaving only the NIR
168 emission of the reference indicator noticeable. As the acidity increases, the pH marker is
169 protonated, which results in a heightened NIR luminescence that is detected along with the
170 emissions of both indicators. The measurement approach uses red excitation light modulated in a
171 sinusoidal manner, leading to a similar modulation of the NIR emission, albeit with a phase
172 discrepancy. This phase variation is registered by the PyroScience OEM module and
173 subsequently converted into a total pH measurement.
174
175 Automatic temperature compensation of the optical pH sensor was achieved using a flexible
176 Teflon-coated temperature probe (Pt100 Temperature Probe, PyroScience GmbH; Fig. 2)
177 soldered onto the OEM module. The optode was placed in a closed flow-through cell directly
178 connected to the underway supply of the ship through which seawater was pumped at a constant
179 rate (6 L/min for SO279 and 9 L/min for SO289; 2.5 m depth) and stirred using a magnetic
180 stirrer (Fig. 2). The entire setup was kept inside a closed box to isolate the optical instrument
181 from any other light source (Fig. 2). All seawater first went through a thermo-salinograph close
182 to the water source, which also measured salinity, temperature and chlorophyll-a fluorescence
183 (chl-a), before going through the pH setup (Fig. 2).
184
185
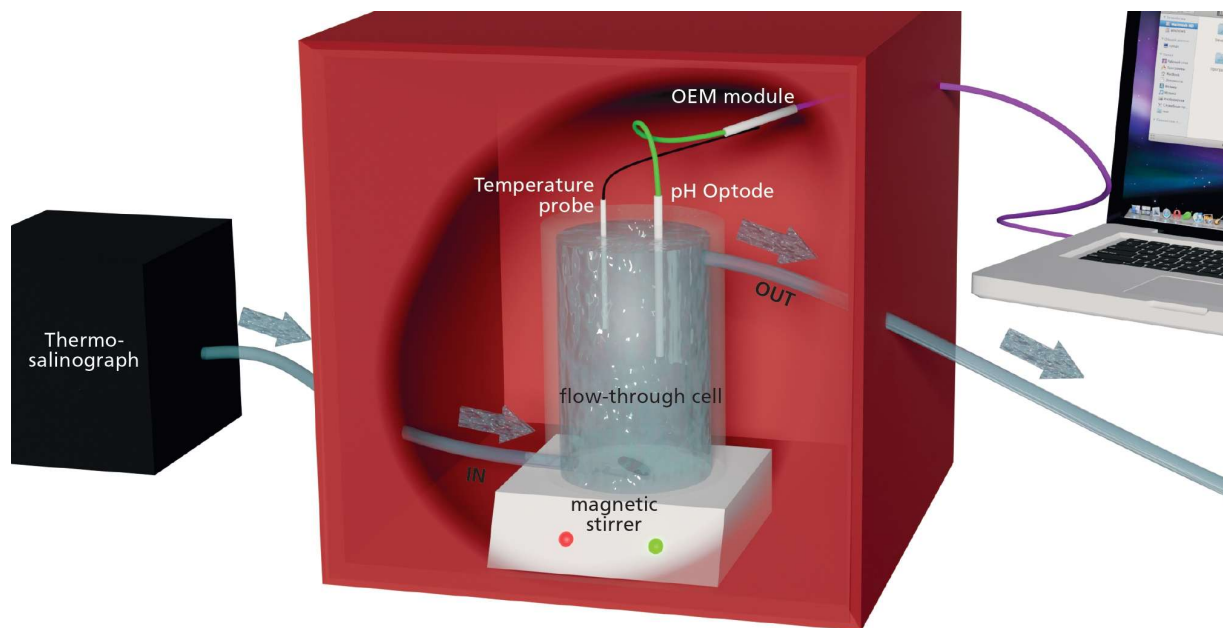
186
187 **Figure 2. Schematic representation of the optical continuous pH measurement system. Arrows indicate the**
188 **direction of flow-through tubing. The system consists of the following components: a thermo-salinograph; a**
189 **flow-through cell; a magnetic stirrer; a fiber-based pH optode; a flexible Teflon-coated temperature probe; a**
190 **fiber-optic meter OEM module Pico-pH-SUB and a portable computer. All elements inside the red box are in**
191 **the dark to avoid any light disturbance.**

2.3 Initial calibration and underway measurements

193 Direct measurements of surface water (~3 m depth) pH were carried out at a frequency of 2
194 measurements min^{-1} for the North Atlantic cruise and 4 measurements min^{-1} for the South Pacific
195 cruise.

196

197 A one-point calibration of the temperature probe was performed against a thermometer inside a
198 water bath (Lauda Ecoline RE106). A two-point calibration of the pH sensor was conducted
199 following the manufacturer's recommended procedure, using PyroScience pH buffer capsules
200 (pH 2 or pH 4 for the acidic calibration point, pH 10 or pH 11 for the basic calibration points).
201 These calibration points deliberately fall far outside the sensor's operating range from pH 7-9 in
202 order to characterize its maximum and minimum responses. Buffers were prepared by dissolving
203 each capsule's powder into 100 mL MilliQ water.

204

205 To further refine the accuracy of the measurements, a pH offset adjustment was applied using
206 certified reference material (CRM, batches #189, #195, and #198; provided by Andrew Dickson,
207 Scripps Institution of Oceanography). Although CRMs do not provide direct certified pH values,
208 we calculated pH_{CRM} from the CRM TA and DIC using the carbonate system equilibrium
209 constants from Lueker et al. (2000). This pH_{CRM} value was then used to adjust the optode-based
210 pH measurements to improve accuracy and align them with discrete observations.
211 To assess the robustness of the pH optode, resolution surface measurements of partial pressure of
212 CO_2 (pCO_2) and pH (samipH) were added as points of comparison. The pH optode, pCO_2 sensor,
213 and samipH sensor were all installed on the same surface seawater supply, which was
214 continuously pumped from approximately 2.5 m depth into the sink of the underway laboratory

215 during the cruise. The PyroScience pH sensor received water from a split of this same supply,
216 ensuring all sensors were sampling the same source water.
217
218 Surface pCO_2 was measured using a factory-calibrated commercial sensor (HydroC, 4H-JENA
219 Engineering GmbH, Germany)(Fietzek et al., 2014) at a 1-minute sampling interval. An
220 automatic zero-point calibration was performed every 6 hours to correct for sensor drift. The
221 recorded pCO_2 values were subsequently adjusted following (Takahashi et al., 2006) to reflect in
222 situ sea surface temperature.
223
224 Surface pH, reported on the total scale, was measured using a factory-calibrated sensor (Sunburst
225 Sensors, USA) at 15-minute intervals. The pH data were calibrated using sea surface salinity and
226 temperature according to the equations provided by Liu et al. (2011) and Millero (2007),
227 respectively.

2.4 Discrete sampling and analysis for other CO_2 parameters

229 The underway seawater system was sub-sampled from the cell every 12 hours via silicone tubing
230 for TA and DIC following an internationally established protocol (Dickson et al., 2007). TA was
231 sampled in Azlon™ HDPE wide neck round 150 mL bottles filled to the neck and poisoned with
232 50 μL saturated $HgCl_2$. DIC was sampled into Labco Exetainer® 12 ml borosilicate vials and
233 poisoned with 15 μL saturated $HgCl_2$. Samples were stored at 4 °C whenever possible and kept
234 in the dark until analysis.
235
236 All TA and DIC analysis was carried out at the Royal Netherlands Institute for Sea Research,
237 Texel (NIOZ). The analysis was calibrated using certified reference material (CRM, batches
238 #189, #195 and #198; provided by Andrew Dickson, Scripps Institution of Oceanography). TA
239 was determined using a Versatile INstrument for the Determination of Total inorganic carbon
240 and titration Alkalinity (VINDTA 3C #017 and #014, Marianda, Germany). The instrument
241 performed an open-cell, potentiometric titration of a seawater subsample with 0.1 M
242 hydrochloric acid (HCl). Results were then recalculated using a modified least-squares fitting as
243 implemented by Calkulate v3.1.0 (Humphreys and Matthews, 2024). DIC concentrations were
244 determined using either the VINDTA system (SO279 samples and part of SO289 samples) or the
245 QuAAtro Gas Segmented Continuous Flow Analyzer (CFA, SEAL Analytical; SO289 samples).
246 Briefly, the VINDTA measures DIC by acidifying a seawater sample, which releases CO_2 that is
247 then quantified through a coulometric titration cell. Similarly, the QuAAtro CFA uses
248 acidification to liberate CO_2, which then discolours a slightly alkaline phenolphthalein pink
249 coloured solution which is measured spectrophotometrically at 520 nm (Stoll et al., 2001).
250
251 For cruise SO279, nutrient samples were gathered using 60 mL syringes made of high-density
252 polyethylene, which were connected to a three-way valve by tubing, drawing directly from the
253 CTD-rosette bottles to avoid air exposure. Immediately upon collection, the samples were taken
254 to the laboratory for processing, where they were filtered through a dual-layer filter with pore
255 sizes of 0.8 and 0.2 μm. All samples were stored at -20°C in a freezer except Si, which were
256 stored at 4°C in a cold room until analysis back at NIOZ. Nutrients were analysed using a
257 QuAAtro Continuous Flow Analyser. Measurements were made simultaneously on four channels
258 together Si, PO_4, NH_4, NO_3, and NO_2. All measurements were calibrated with standards diluted
259 in low nutrient seawater (LNSW) in the salinity range of the stations (approx. 34 – 37) to ensure

260   that analysis remained within the same ionic strength. Prior to analysis, all samples were brought
261   to laboratory temperature in about one to two hours. To avoid gas exchange and evaporation
262   during the runs with NH_4 analysis, all vials including the calibration standards were covered with
263   Parafilm under tension before being placed into the auto-sampler, so that the sharpened sample
264   needle easily penetrated through the film leaving only a small hole. Silicate samples were
265   measured separately on a TRAACS Gas Segmented Continuous Flow Analyser (manufactured
266   by Bran+Lubbe, now SEAL Analytical) following Strickland and Parsons (1972). A sampler rate
267   of 60 samples per hour was also used for all analyses. Calibration standards were diluted from
268   stock solutions of the different nutrients in 0.2 μm filtered LNSW diluted with de-ionised water
269   to obtain approximately the same salinity as the samples and were freshly prepared every day.
270   This diluted LNSW was also used as the baseline water for the analysis and in between the
271   samples. Each run of the system had a correlation coefficient of at least 0.9999 for 10 calibration
272   points. The samples were measured from the lowest to the highest concentration, i.e., from
273   surface to deep waters in order to reduce carry-over effects. Concentrations were recorded in μM
274   at an average container temperature of 23.0 °C and later converted to μmol/kg by dividing the
275   recorded concentration by the sample density, calculated following Millero and Poisson (1981).
276
277   For cruise SO289, nutrient analysis was carried out on seawater from every Niskin bottle
278   triggered at various depths during each cast. The seawater was transferred into 15 mL
279   polypropylene vials. Each container and its cap were rinsed three times with seawater before
280   filling. If immediate analysis was not possible, samples were stored in a fridge at 4 °C in the
281   dark. Macro nutrients were analyzed onboard using a segmented flow injection analysis with a
282   Seal Analytical QUAATRO39 auto-analyzer that includes an XY2-autosampler. For nanomolar
283   nutrient analysis, a modified setup with 1000 mm flow cells was employed. The setup was
284   designed to analyze four channels: total oxidized nitrogen (TON), silicate, nitrite, and phosphate,
285   using methods outlined in QuAAtro Applications: Method Nos. Q-068-05 Rev. 11, Q-066-05
286   Rev. 5, Q-070-05 Rev. 6, and Q-064-05 Rev. 8, respectively. To ensure analytical consistency
287   and validate the data, each run was checked against Certified Reference Material for Nutrients in
288   Seawater (RMNS). Nutrient analyses were further validated using KANSO CRM, with specific
289   lot numbers for macromolar and nanomolar nutrient concentrations.
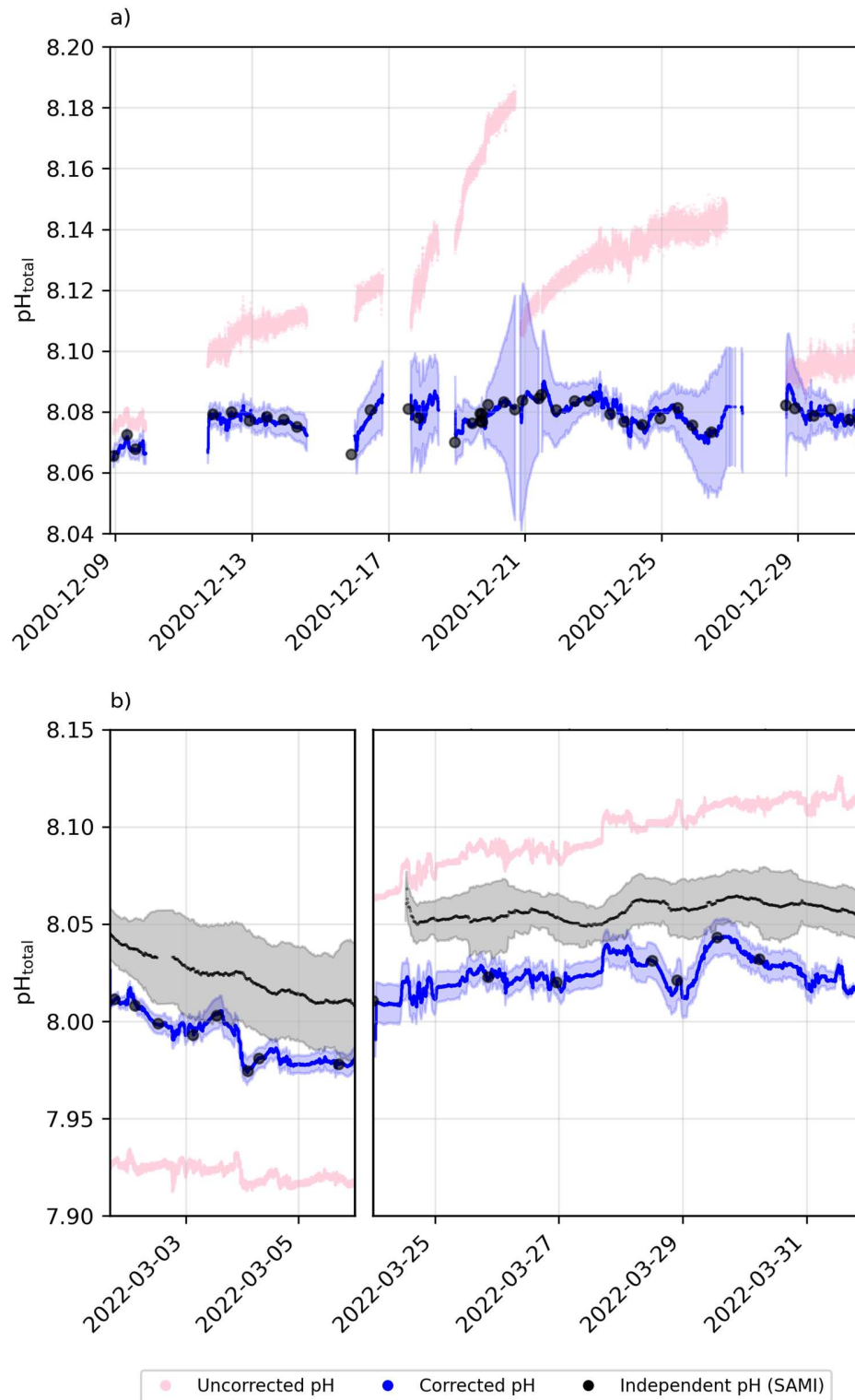
290
291 **Figure 3. Underway pH drift correction using pH$_{total(TA/DIC)}$ subsamples for a) cruise SO279 and b) cruise**
292 **SO289. Raw pH measurements (pink); corrected pH values and uncertainty from bootstrapping (blue);**
293 **subsample pH$_{total(TA/DIC)}$ depicted as black circles. Independent pH from the SAMI sensor is shown in black**
294 **for the South Pacific cruise (SO289).**

2.5 Post-cruise correction

To ensure the reliability of the dataset, an initial screening was conducted to identify and flag unreliable continuous pH data points, primarily attributable to optode stabilization issues. Specifically, data points recorded during documented periods of particularly rough weather, when air intrusion into the underway system was reported, were flagged as unreliable due to the resulting abrupt and erratic drift patterns inconsistent with expected optode and surface ocean pH behavior.

pH_{obs} was calculated from TA and DIC UWS discrete samples) using PyCO2SYS (Version 1.8.2; (Humphreys et al., 2022)), with the carbonic acid dissociation constants of Lueker et al. (2000), the bisulfate dissociation constant of Dickson (1990), the total boron to chlorinity ratio of Uppström (1974), and the hydrogen fluoride dissociation constant of Dickson and Riley (1979).These calculated values were then aligned with the continuous pH dataset to determine the offset between pH_{obs} subsamples and the continuous optode-based pH measurements (Fig. 3). A Piecewise Cubic Hermite Interpolating Polynomial (PCHIP; (Fritsch & Carlson, 1980) was fitted to the offset as a way to continuously correct pH variations across the entire pH timeseries (Fig. 3). While continuous recalibration of the optode was not possible, a two-point calibration, supplemented by a third-point correction using a CRM, was performed prior to deployment (see Section 2.3). Additionally, discrete underway TA and DIC samples, collected twice daily when possible, were used to assess and correct for drift in the optode measurements. The manufacturer specifies a drift of <0.005 pH units per day at 25 °C, though drift may vary slightly with temperature. During our deployments, seawater temperatures ranged from 13.4°C to 22.0 °C in the North Atlantic and from 19.8°C to 27.7 °C in the South Pacific. While the cooler North Atlantic conditions may have reduced drift rates slightly, temperatures during the South Pacific cruise were close to or above 25 °C for extended periods, and full manufacturer-specified drift is likely to have occurred. Even if drift remained at the nominal rate of 0.005 pH units per day, this would amount to a cumulative offset of up to 0.175 pH units over ~5 weeks (SO279) and 0.28 pH units over ~8 weeks (SO289), in line with the deviation observed in our raw data (Fig. 3). Notably, even with a recalibration during the cruise, drift before and after that point would still introduce offsets. Thus, over timescales of days and longer, the accuracy of the measurement is dependent on the correction to the TA and DIC samples.

To further assess the robustness of our drift correction, we compared our optode-corrected pH and derived fCO_2 values with independent continuous measurements from autonomous sensors (Figs. S1 and S2). The corrected optode pH exhibited a lower mean deviation (~0.008) from discrete pH (TA/DIC) measurements than the independent spectrophotometric SAMI sensor (~0.02 pH units), indicating that our correction effectively minimized drift-related inaccuracies (Fig. S1). The overall scatter between the optode-corrected and SAMI-measured pH was modest (RMSD = 0.0329), suggesting reasonable consistency despite inherent sensor measurement noise. Similarly, calculated fCO_2 from corrected optode pH showed a larger mean deviation (~12.7 µatm) compared to directly measured fCO_2 (~5 µatm; Fig. S2). The relatively higher RMSD (30.76 µatm) reflects variability in calculated fCO_2 arising from uncertainties in alkalinity estimates and carbonate system calculations rather than fundamental flaws in the optode pH correction itself (Fig. S2). Thus, these validations collectively confirm that our corrected pH data represent a reliable improvement over raw optode measurements, suitable for robust biogeochemical analysis.

341

342   The overall post-cruise correction of pH involved an adjustment of approximately 0.4 to bring
343   the continuous measurements in line with discrete carbonate system observations. However,
344   despite this magnitude of correction, the internal variability within each cycle remains robust,
345   with observed diel fluctuations consistently within ~0.01. This fine-scale variability aligns with
346   expected temperature-driven pH changes and is distinguishable from random noise. The
347   measurement uncertainty of ~ ±0.01 means that while some small-scale variations approach the
348   uncertainty threshold, the structured nature of the observed diel trends—rather than random
349   scatter—supports their validity. If these variations were purely noise, we would not expect to see
350   systematic agreement with temperature fluctuations across multiple cycles and regions. To
351   further assess the robustness of these signals, we conducted a signal-to-noise ratio (SNR)
352   analysis (see Supplementary Information). SNR values exceeded 1 when pH was modeled based
353   on temperature (and salinity) in the North Atlantic, indicating that observed diel variability
354   surpassed measurement noise and reflected true environmental signals. In contrast, SNR values
355   remained below 1 in the South Pacific, suggesting that pH variability there was closer to the
356   uncertainty threshold and less clearly distinguishable from noise.

357   **2.6 Estimation of other biogeochemical parameters**

358   TA was estimated for the continuous pH dataset using the empirical equations presented by Lee
359   et al. (2006). For the North Atlantic, the corresponding equation was used (see Fig. S3 in
360   supplementary information):
361

$$TA_{NA} = 2305 + 53.97(SSS - 35) + 2.74(SSS - 35)^2 - 1.16(SST - 20) \\ + 0.040(SST - 20)^2 \tag{1}$$

362   In contrast, the (Sub)tropics equation (SBT, Eq. 2) was applied for the South Pacific region, as
363   the cruise mostly followed the 32.5°S longitude and this equation was determined to offer the
364   best fit to the local temperature (SST) and salinity (SSS) equation (see Fig. S3 in supplementary
365   information):
366

$$TA_{SBT} = 2305 + 58.66(SSS - 35) + 2.32(SSS - 35)^2 - 1.41(SST - 20) \\ + 0.040(SST - 20)^2 \tag{2}$$

367
368   TA estimates were used together with pH to solve the rest of the marine carbonate system (i.e.
369   DIC and fCO$_2$) using PyCO2SYS (Version 1.8.2; (Humphreys et al., 2022), with the carbonic
370   acid dissociation constants of Lueker et al. (2000), the bisulfate dissociation constant of Dickson
371   (1990), the total boron to chlorinity ratio of Uppström (1974), and the hydrogen fluoride
372   dissociation constant of Dickson and Riley (1979).
373
374   While direct TA measurements were collected twice daily, their limited temporal resolution
375   made them unsuitable for continuous carbonate system calculations. The empirical TA equations
376   from Lee et al. (2006) provided a high-resolution dataset that allowed for more comprehensive
377   system reconstructions. A comparison of measured and estimated TA values (see Fig. S3 in
378   supplementary information) shows good agreement, with deviations generally within the
379   uncertainty of carbonate system calculations.

380 **2.7 Projected pH variability**

381 The derived parameters pH_{temp}, pH_{sal}, and $pH_{temp,sal}$ were calculated while holding TA and DIC
382 constant at the average values of each diel cycle, where TA was estimated following Lee et al.
383 (2006) and DIC was derived from measured underway pH and estimated TA. This approach
384 allowed us to assess the expected pH response to changes in temperature and salinity alone,
385 without introducing additional assumptions about concurrent variations in carbonate chemistry.
386
387 Similarly, $pH_{TA,fCO2}$ was computed while holding TA and fCO_2 constant at their daily mean
388 values. fCO_2 was derived from measured pH and estimated TA, ensuring that the calculation
389 reflects equilibrium conditions for given waters with distinct temperature-salinity properties
390 while allowing temperature and salinity to vary independently. This formulation enables direct
391 comparisons of observed pH to expected values under different scenarios, helping to disentangle
392 the relative influences of abiotic drivers (temperature, salinity) versus processes such as air-sea
393 CO_2 exchange and biological activity.
394
395 Our approach maintains consistency by using a single set of carbonate chemistry parameters (TA
396 and DIC) as the baseline for assessing temperature and salinity influences. While pH is initially
397 used to estimate DIC, the subsequent calculations isolate the effects of temperature and salinity
398 without assuming variability in TA or DIC. This method enables direct comparisons between
399 observed and expected pH, providing a clearer framework for distinguishing abiotic influences
400 from biological processes and air-sea CO_2 exchange.
401
402 All calculations were done using the same configuration in PyCO2SYS described in Sect. 2.6.

403 **2.8 Identification of full diel cycles**

404 To account for the influence of geographic location on temporal measurements, timestamps from
405 Coordinated Universal Time (UTC) were converted to Local Solar Time (LST). This conversion
406 was necessary to align time-sensitive data with the true solar position at each measurement
407 location, thereby facilitating more accurate comparisons of environmental data across different
408 geographic regions and improving the analysis of diel processes.
409
410 The conversion process involved calculating the mean longitudinal position for each date within
411 the dataset. Subsequently, a time offset was determined based on the average longitude,
412 assuming a standard rate of Earth's rotation. This offset was then applied to the original UTC
413 timestamps, resulting in a modified dataset with timestamps adjusted to reflect LST:
414

$$\text{DateTime}_{\text{LST}} = \text{DateTime}_{\text{UTC}} + \left(\frac{\text{Longitude}_{\text{mean}}}{15}\right). \tag{3}$$

415 Following the conversion to LST, the dataset was further processed to isolate complete diel
416 cycles to ensure that only data representing full 24-hour cycles were included. The North
417 Atlantic dataset included 7 complete diel cycles, while the South Pacific dataset included 11
418 complete diel cycles.

2.9 Uncertainty propagation

2.9.1 Uncertainty in pH measurements and post-correction

To provide a comprehensive uncertainty estimate, we considered multiple sources of potential error. The manufacturer-reported accuracy (±0.05 for pH 7.5–9.0, ±0.1 for pH 7.0–7.5) represents a systematic bias that was addressed through calibration against discrete CRM samples and is not appropriate for inclusion as a random uncertainty. Likewise, the reported precision (±0.003 at pH 8.0) reflects the repeatability of the measurements but does not quantify the full range of uncertainty for error propagation. The final uncertainty in pH measurements was estimated by combining uncertainties from two main sources: (1) the uncertainty in the TA and DIC measurements used to calculate pH_{obs} and (2) the correction of the UWS pH measurements using pH_{obs}

First, the precision in TA and DIC were determined based on the RMSE from repeated measurements of a known standard water sample in the laboratory (NIOZ; 0.92 umol/kg and 1.95 μmol/kg, respectively). Then a Monte Carlo simulation was applied to the calculated pH_{obs} to obtain a pH_{RMSE} for each subsample pH_{obs}.

Next, the pH measurements obtained from the optode were corrected using $pH_{(TA, DIC)}$ from the discrete measurements of TA and DIC. The uncertainty in the pH correction was assessed using a bootstrapping approach (n=1000 iterations), where a fraction (50%) of the discrete samples was randomly omitted in each iteration and the selected fraction of the discrete samples varied within its own pH_{RMSE}.

The variation in each subsample's pH_{obs} captured the likely variability in TA and DIC measurements, while omitting different subsets of data allowed for the estimation of how sensitive the pH correction is to which set of subsamples are used for calibration.

2.9.2 Uncertainty in pH diel patterns

To ensure the observed patterns in pH over the full 24-hour cycles were not artifacts of sampling bias or other anomalies, a Monte Carlo simulation (n = 1000 iterations) was employed on each diel cycle's hourly data analysis. This simulation randomly selected 50% of the data points for each hour (i.e. 50% of 120 hourly measurements for the North Atlantic dataset and 50% of 240 hourly measurements for the South Pacific dataset), repeatedly calculating the mean pH to assess the consistency and robustness of the hourly trends. This component of the uncertainty proved insignificant (i.e., errors bars were smaller than the symbols in Fig. 4 and 5).

2.10 CO$_2$ air-sea flux dynamics

Air-Sea CO$_2$ fluxes were computed based on the relationship:

$$F = k_w \times K_0 \times (pCO_{2_{sw}} - pCO_{2_{air}}) \tag{4}$$

where F represents the flux of CO$_2$ across the air-sea interface, k_w is the gas transfer velocity, K_0 is the solubility constant and $pCO_{2_{sw}}$ is the partial pressure of CO$_2$ in sea water, representing the concentration of dissolved CO$_2$ that is in equilibrium with the atmosphere and $pCO_{2_{air}}$ is the

460   partial pressure of CO_2 in the atmosphere above the ocean surface. For the fluxes, a positive
461   value shows the ocean acts as a source (i.e., releasing CO_2 to the atmosphere), while a negative
462   value shows it acts as a sink (i.e., absorbing CO_2 from the atmosphere). The parameterisation
463   from Ho et al. (2006) was used to determine the gas transfer velocity. All fluxes were computed
464   using the pySeaFlux package (v2.2.2; (Fay et al., 2021).
465
466   Flux calculations were performed for each complete diel cycle, followed by the computation of
467   the mean flux for each cycle. Additionally, the mean flux for the diel cycle was also calculated
468   from the daily mean inputs (wind speed, temperature, salinity, and pCO_2), and specifically
469   computed for the hours 12 AM and 12 PM (LST) to examine temporal variations within each
470   cycle (Fig. 9).

471
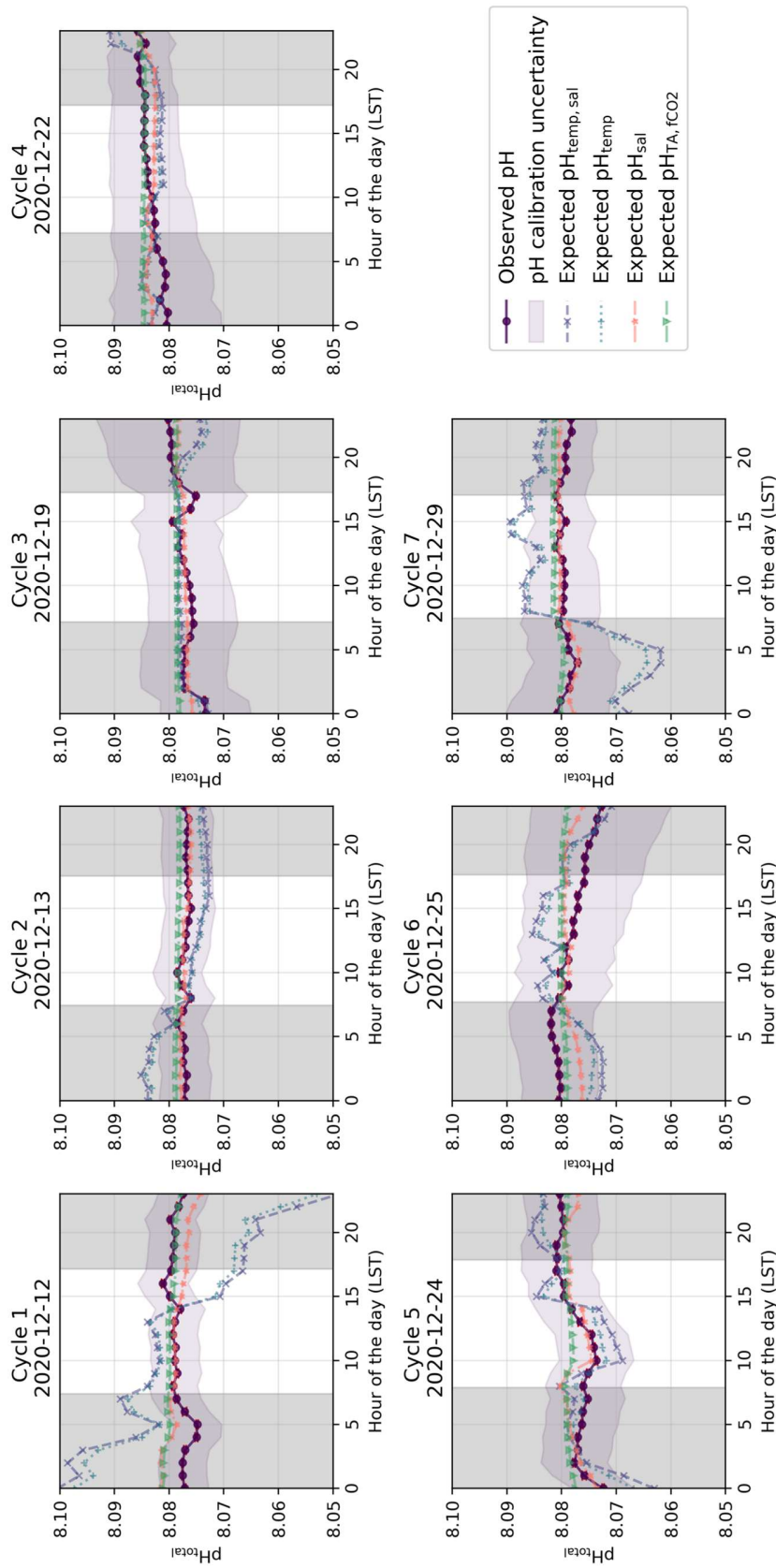
Figure 4. Identified diel cycles for cruise SO279 in the North Atlantic Ocean. Dark purple lines show observed pH (pH$_{obs}$), dashed grey lines show mean observed pH over the full diel cycle, and black lines show overall mean pH for all diel cycles combined for that cruise. The remaining shows expected pH using varying temperature and salinity (pH$_{temp,sal}$; dashed light purple lines), varying temperature alone (pH$_{temp}$; dashed blue lines), varying salinity alone (pH$_{sal}$; dashed orange lines) and constant TA and fCO$_2$ (pH$_{TA,fCO2}$; dashed green lines). Grey areas are night hours.

472
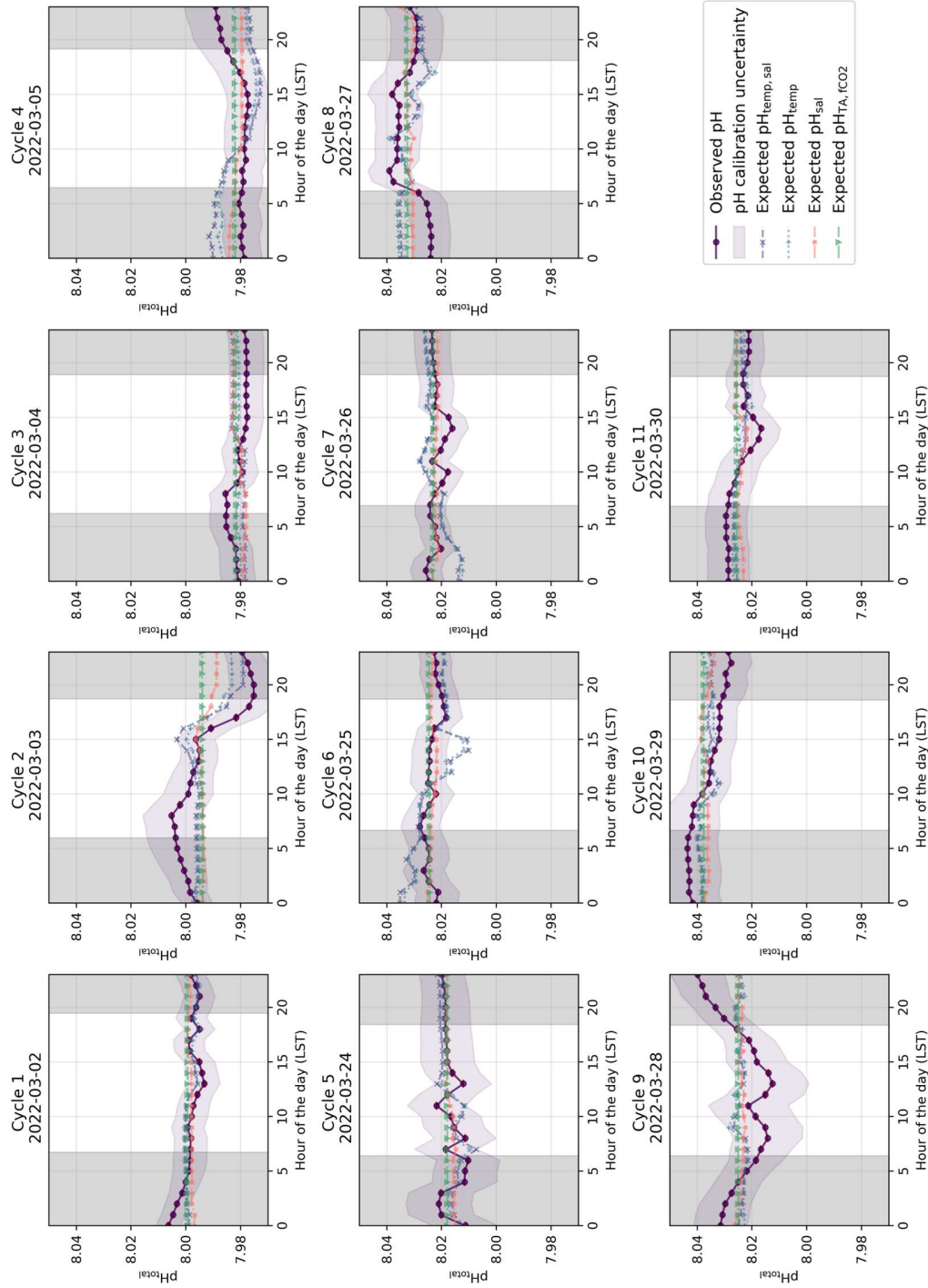
Figure 4. Identified diel cycles for cruise SO289 in the South Pacific Ocean. Dark purple lines show observed pH (pH$_{obs}$), dashed grey lines show mean observed pH over the full diel cycle, and black lines show overall mean pH for all diel cycles combined for that cruise. The remaining shows expected pH using varying temperature and salinity (pH$_{temp,sal}$; dashed light purple lines), varying temperature alone (pH$_{temp}$; dashed blue lines), varying salinity alone (pH$_{sal}$; dashed orange lines) and constant TA and fCO$_2$ (pH$_{TA,fCO2}$; dashed green lines). Grey areas are night hours.
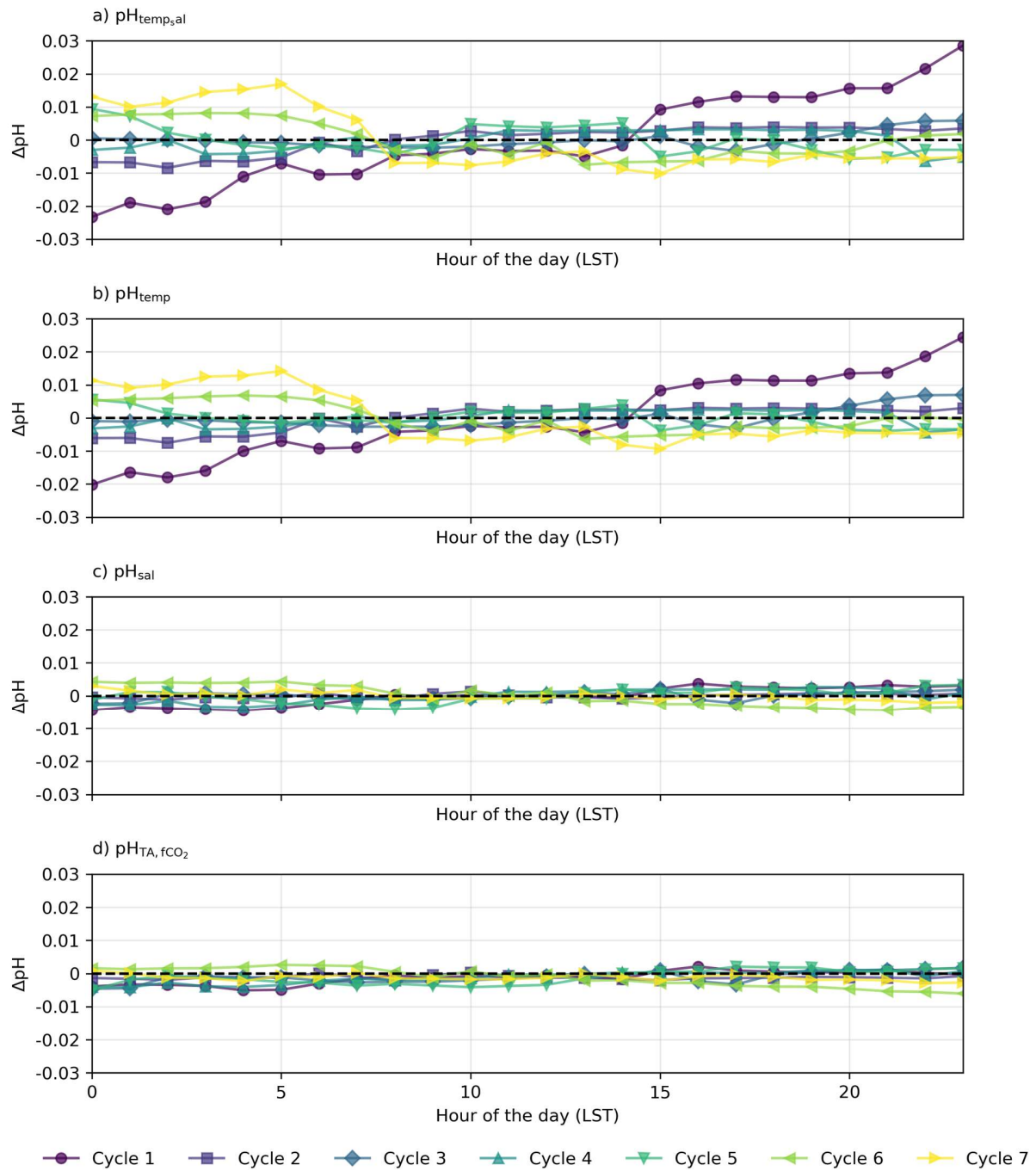
473
474
475 **Figure 6. Residual plots for diel cycles in the North Atlantic, illustrating the differences (ΔpH) between**
476 **observed pH measured by the optode (pH$_{obs}$) and a) pH calculated from constant TA and DIC with varying**
477 **temperature and salinity (pH$_{temp,sal}$), b) varying temperature only (pH$_{temp}$), c) varying salinity only (pH$_{sal}$) and**
478 **d) constant TA and fCO$_2$ with varying temperature and salinity . Horizontal dashed lines at y=0 indicate no**
479 **deviation between observed and calculated pH.**

480
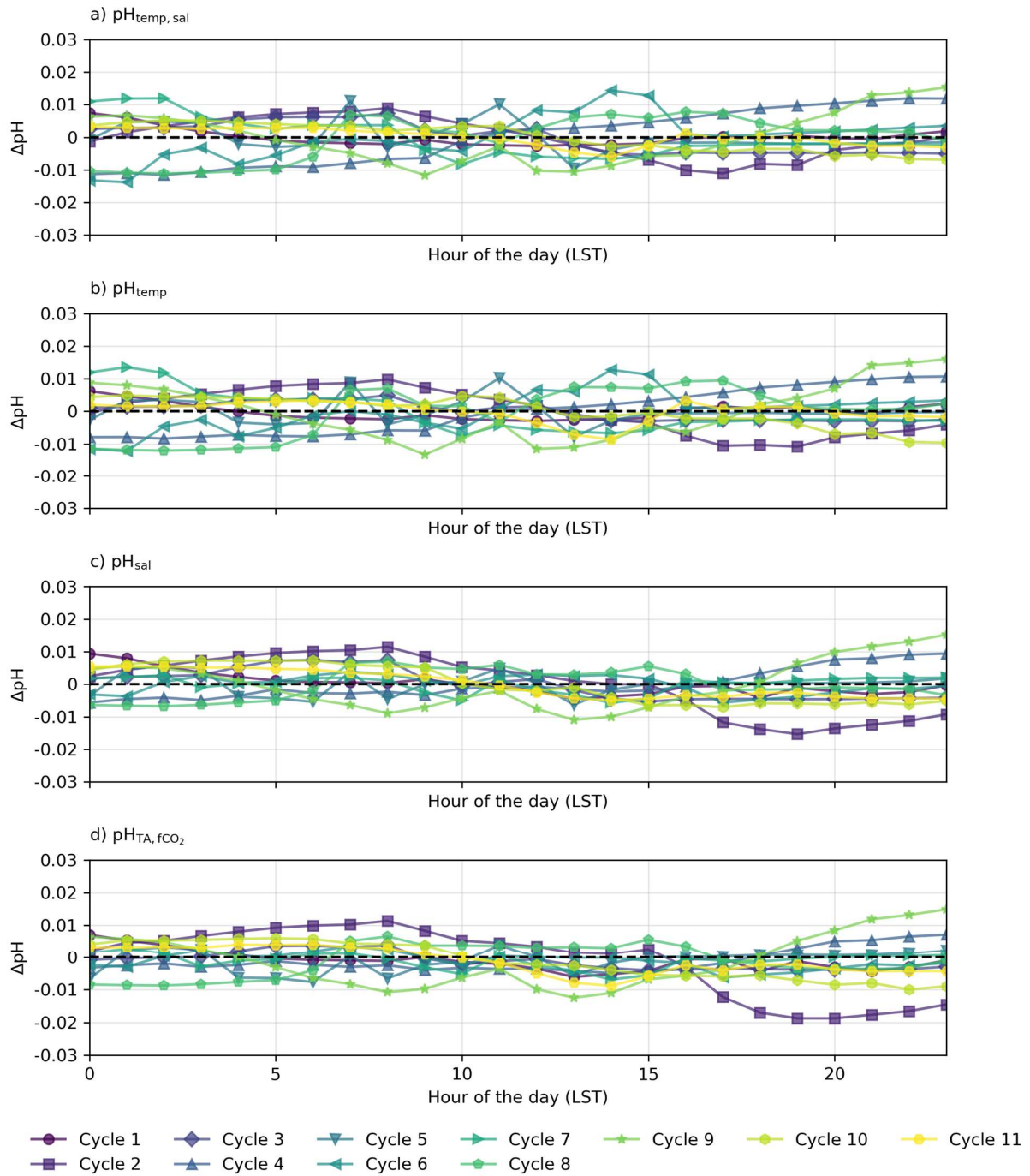
481
482
483 **Figure 7. Residual plots for diel cycles in the South Pacific, illustrating the differences (ΔpH) between**
484 **observed pH measured by the optode (pH$_{obs}$) and a) pH calculated from constant TA and DIC with varying**
485 **temperature and salinity (pH$_{temp,sal}$), b) varying temperature only (pH$_{temp}$), c) varying salinity only (pH$_{sal}$) and**
486 **d) constant TA and fCO$_2$ with varying temperature and salinity . Horizontal dashed lines at y=0 indicate no**
487 **deviation between observed and calculated pH.**

488
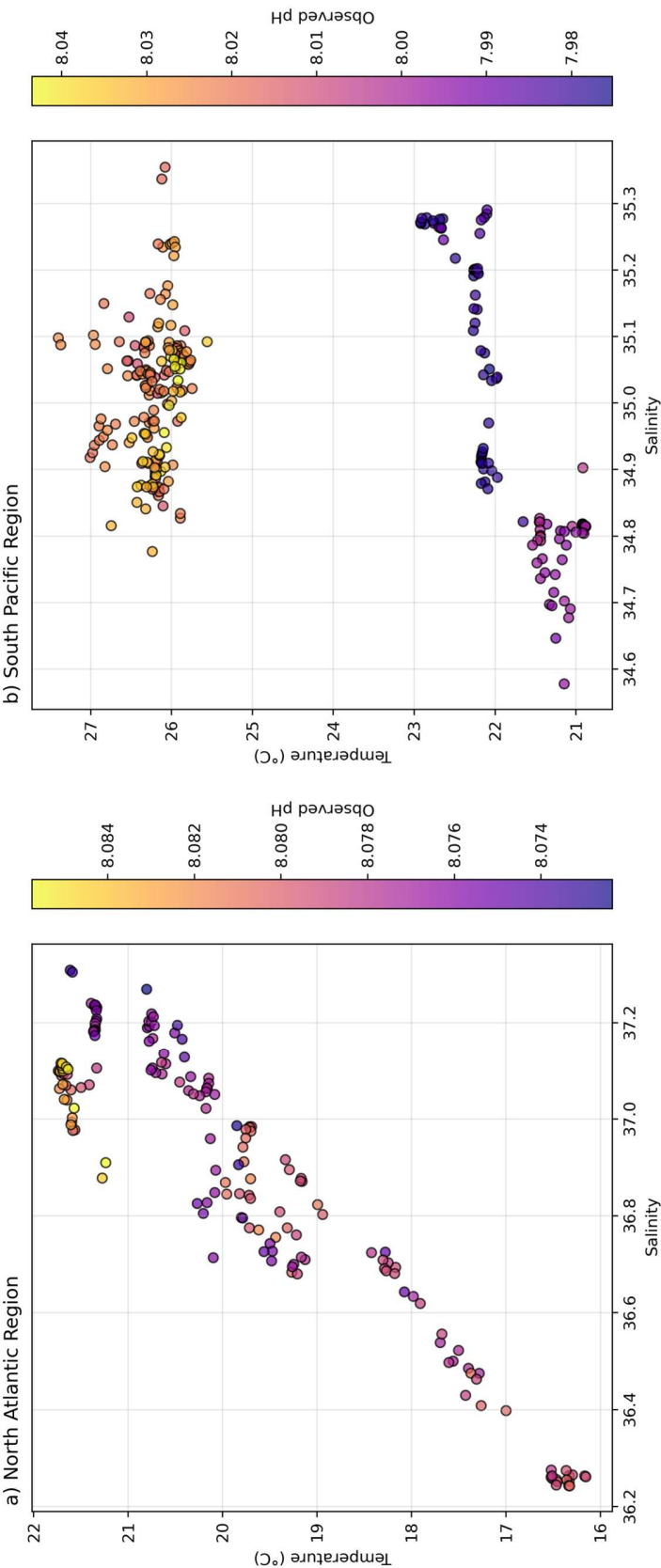
Figure 8. T/S diagram with observed pH for a) the North Atlantic region and b) the South Pacific region.

489
490 **Figure 9. Sensitivity analysis of mean CO$_2$ flux compared to flux calculated from mean inputs, fluxes for 12**
491 **AM (LST) and fluxes for 12 PM (LST). Top panel a) shows cruise SO279 in the North Atlantic while bottom**
492 **panel b) shows cruise SO289 in the South Pacific.**

493 **3 Results and Discussion**

494 We first analyse the effects of temperature and salinity on pH across different diel cycles and
495 regions (Sect. 3.1) using high-resolution pH data enabled by our novel optical measurement
496 system. We examine the pH expected from temperature and salinity variations alone (pH$_{temp,sal}$),
497 disregarding changes in TA or DIC. If pH$_{obs}$ (i.e. corrected underway pH measurements using
498 discrete TA and DIC subsamples) aligns with pH$_{temp,sal}$, it suggests that recent temperature
499 changes, such as day-night cycles, primarily control pH. In this context, "recent" is relative to the
500 air-sea CO$_2$ equilibration timescale, i.e., temperature change that happened recently enough that
501 its effect on pH has not been modified by subsequent gas exchange. Next, we assess the
502 influence of hydrographic variations on pH by considering pH$_{TA,fCO2}$, which accounts for
503 constant fCO$_2$ instead of DIC alongside constant TA and varying temperature and salinity.
504 Alignment of pH$_{obs}$ with pH$_{TA,fCO2}$ indicates that slower or long-ago processes control pH. For
505 example, an observed change in temperature may be due to spatial variability, with the ship
506 passing through different waters with distinct temperature-salinity properties that have had
507 different temperatures for long enough to reequilibrate with atmospheric CO$_2$. By leveraging the
508 high-frequency resolution of our measurement system, we then explore the role of biological
509 activity and its interaction with abiotic factors by looking at the discrepancies between pH$_{obs}$ and
510 both pH$_{temp,sal}$ and pH$_{TA,fCO2}$ (Sect. 3.2). Finally, we distinguish between temporal and spatial
511 variability in our measurements (Sect. 3.3), considering implications for air-sea CO$_2$
512 equilibration timescales at fine spatio-temporal scales (Sect. 3.4).

513 **3.1 Influence of temperature and salinity**

514 **3.1.1 Basin-scale comparison**

515 The diel cycles of pH observed in the North Atlantic and South Pacific Oceans are significantly
516 influenced by temperature. In the North Atlantic, observed pH stays within ±0.01 of pH$_{temp,sal}$,
517 supporting the role of temperature and salinity in driving pH changes (Fig. 6). However, in the
518 South Pacific, where SNR values for temperature and salinity-driven pH changes remain below
519 1, observed fluctuations may not exceed measurement noise, making it uncertain whether these
520 variations reflect true environmental signals or instrument variability (Fig. 7; Table S2 in
521 Supplementary Information). . Despite this, the systematic nature of diel fluctuations—seen
522 across multiple cycles and their correlation with expected temperature-driven trends—suggests
523 they are meaningful rather than random variability.

524
525 Salinity alone does not appear to strongly influence pH in any observed cycle. For both ocean
526 basins, pH$_{sal}$ typically remains close to the mean pH of each cycle, rather than impacting the
527 observed pH significantly. This consistency suggests that daily salinity variations do not exert a
528 primary influence on the observed pH (Fig. 4 and 5; Fig. 6c; Fig. 7c; Tables S1 and S2 in
529 Supplementary Information). Thus, the rest of this section focuses on the effect of temperature
530 on the observed pH.
531

532

533 In the North Atlantic, the observed variability in pH generally matches the calculated pH_{temp} and
534 $pH_{temp,sal}$, with most cycles' residuals within ±0.01 (Fig. 4 and Fig. 6a and b, Cycles 2, 3, 4, 5 and
535 6). This agreement suggests that temperature and salinity together explain most of the observed
536 short-term variations. However, some cycles show more pronounced deviations. Cycle 3
537 demonstrates a particularly strong alignment between observed pH and expected $pH_{temp,sal}$
538 throughout the day (mean residuals < 0.001; Fig. 4; Fig. 6a and b), while Cycle 4 also exhibits
539 minimal variation (residuals -0.007 to 0.003; Fig. 4).

540

541 In the South Pacific, pH variability follows a different pattern, While some cycles (eg. Cycles 1,
542 3, 4, and 6) show a similar agreement between observed pH and $pH_{temp,sal}$ (Fig. 5), overall, the
543 influence of temperature appears weaker than in the North Atlantic. The SNR analysis (see Text
544 S1 in Supplementary Information) confirms this, with North Atlantic temperature-driven pH
545 fluctuations exceeding noise (SNR = 1.39 for $pH_{temp,sal}$, 1.20 for pH_{temp}), while all pH variations
546 in the South Pacific remain below SNR = 1 (see Tables S1 and S2 in Supplementary
547 Information). This suggests that in the South Pacific, observed fluctuations may be more
548 influenced by noise than by real temperature-driven variability. However, the persistence of
549 systematic diel fluctuations suggests that meaningful signals are still present.

550

551 The physical oceanographic context of each basin likely contributes to these differences. In the
552 North Atlantic, significant mixing due to ocean currents, eddies, and upwelling introduces
553 substantial variability in temperature, salinity, and pH across different waters with distinct
554 temperature-salinity properties (Fig. 6a and b; see Fig. S6 in Supplementary Information). The
555 Gulf Stream and North Atlantic Drift contribute to this complexity, which may help maintain
556 stronger temperature-driven pH changes by continuously exposing surface waters to variable
557 thermal forcing (Liu & Tanhua, 2021). In contrast, the South Pacific exhibits more predictable
558 hydrographic dynamics, driven largely by advection and mixing within large-scale gyres and
559 trade wind systems (Vallis, 2017). This results in a more stable and homogeneous water column,
560 where observed pH fluctuations remain closer to the measurement uncertainty (Fig. 7).**3.1.2 Diel**
561 **pH variability**Beyond the basin-scale differences, a key feature of the observed pH cycles is the
562 variability between daytime and nighttime conditions. In both basins, temperature changes
563 between day and night are expected to drive corresponding pH shifts due to the temperature
564 dependence of the carbonate system.

565

566 In the North Atlantic, observed pH generally follows expected temperature-driven changes, with
567 pH_{temp} and $pH_{temp,sal}$ showing higher values at night and lower values during the day due to the
568 inverse relationship between temperature and pH (Fig. 4, Fig. 6). For example, in Cycles 3 and 6,
569 the residuals between observed and expected pH remain small throughout the day, reinforcing
570 the dominance of temperature as a control mechanism. However, in some cycles (e.g., Cycle 1),
571 nighttime pH remains elevated beyond what would be expected from temperature alone,
572 suggesting the influence of additional processes such as biological activity or air-sea CO_2
573 exchange.

574

575 In the South Pacific, similar diel patterns are present but exhibit greater variability across cycles.
576 Some cycles (e.g., Cycle 8) show clear daytime decreases and nighttime increases in pH,
577 consistent with temperature-driven changes (Fig. 5). However, in other cases (e.g., Cycle 9),

578 observed pH departs from the expected diel pattern, indicating that other factors may be
579 influencing short-term variability.
580
581 The persistence of nighttime pH anomalies in both basins raises questions about equilibration
582 timescales. While temperature-driven changes in pH and fCO$_2$ occur rapidly in response to
583 solubility and speciation shifts, CO$_2$ equilibration between the atmosphere and ocean occurs over
584 much longer timescales (weeks to months; (Jones et al., 2014)). This means that pH adjustments
585 due to temperature occur almost instantly, but whether they persist over a full diel cycle depends
586 on the history of the hydrographic properties. If waters have recently equilibrated with the
587 atmosphere, its pH should closely follow pH$_{temp,sal}$. However, if these waters have undergone
588 rapid temperature shifts without sufficient time for equilibration, observed pH may diverge from
589 temperature-based expectations. This highlights the interplay between rapid thermodynamic
590 effects and longer equilibration processes, particularly in regions like the North Atlantic, where
591 mixing introduces additional complexity.
592
593 Ultimately, our observations suggest that while temperature is a dominant driver of diel pH
594 changes, the extent to which these changes persist overnight depends on the physical
595 characteristics of the surface waters and their equilibration history. In the North Atlantic, where
596 mixing is more dynamic, the system appears to re-equilibrate more readily, whereas in the South
597 Pacific, longer equilibration timescales may contribute to greater deviations from expected pH
598 patterns.
599

3.2 Influence of biological activity

601 While temperature and salinity effects on pH have been addressed in Sect. 3.1, deviations from
602 expected patterns may be shaped by biological processes. The process of photosynthesis during
603 daylight consumes CO$_2$, leading to a rise in pH, whereas respiration and decomposition at night,
604 which release CO$_2$, lower pH (Falkowski, 1994; Falkowski & Raven, 2013). The balance
605 between photosynthesis and respiration hence affects pH, and should result in a diel pH cycle.
606 However, biological signals in the open ocean are often weaker than in coastal or upwelling
607 regions due to lower phytoplankton biomass and primary production rates (Behrenfeld &
608 Falkowski, 1997; Johnson et al., 2010). As a result, strong diel biological pH signals are not
609 typically expected in oligotrophic oceanic waters. These biological processes can also influence
610 the rate at which CO$_2$ equilibrates between the ocean and atmosphere. For instance, intense
611 photosynthetic activity during daylight hours can rapidly deplete seawater pCO$_2$ in surface
612 waters, potentially accelerating seawater CO$_2$ uptake from the atmosphere. Conversely,
613 nighttime respiration can increase pCO$_2$, slowing the outgassing process and thus extending the
614 equilibration timescale. However, given an equilibration timescale of months, these day and
615 night changes likely get averaged out over longer periods, resulting in an overall steady-state
616 CO$_2$ flux and pH when observed over longer temporal scales.
617
618 These biological processes are particularly evident in some cycles from the North Atlantic where
619 the expected pH$_{temp,sal}$ changes due to temperature and salinity do not align with the observed
620 data, but do follow the distribution expected from biological activity (Fig. 4).). However, the
621 strength of these pH variations should be interpreted with caution, as biological activity in open-
622 ocean regions tends to be relatively low (Longhurst, 2010). The North Atlantic subtropical gyre,

623   for instance, has low rates of primary productivity (Baines et al., 1994; Tilstone et al., 2003),
624   which suggests that biological-driven pH variations would be relatively small. This is especially
625   evident for Cycle 1, which shows an increase in pH during daylight hours and a decrease in pH
626   during night hours, with a peak in pH in late afternoon and the lowest pH occurring in the early
627   morning before sunrise (Fig. 4). Other cycles likely reflect the combined impact of biological
628   processes and temperature effects, as the observed pH does not fully align with the distribution
629   expected from any of temperature, salinity or biological activity (Fig. 4 and 6). In the South
630   Pacific Ocean, some cycles show significant variability within pH_{obs} that are not mirrored by the
631   expected $pH_{temp,sal}$ changes (Fig. 5, Cycles 2, 8). For example, Cycle 2 exhibits significant
632   deviations in pH with higher observed values in the morning and a drop in the afternoon (Fig. 5).
633   Although this suggests a potential biological influence, the SNR values remain below 1 across all
634   expected pH estimates, making it unclear whether the observed fluctuations are truly driven by
635   biological activity or simply fall within the instrument's noise threshold (Table S2 in
636   Supplementary Information).
637

638   The interplay between photosynthesis during the day and respiration at night, with possible
639   contributions of other biological processes, may be behind the more pronounced peaks and
640   troughs of Cycles 2 and 9 (Fig. 6; Duarte and Agusti (1998). Nitrogen fixation consumes
641   hydrogen ions, increasing pH, whereas denitrification releases hydrogen ions, thereby decreasing
642   pH (Richardson, 2000; Zehr & Kudela, 2011). However, without nutrient and oxygen data, we
643   cannot directly assess whether these processes also impacted the observed pH.
644

645   Although biological activity likely accounts for some variability, not all cycles exhibit the same
646   residual, presumably biotic pattern of variation (Fig. 4 and 5). This aligns with expectations, as
647   phytoplankton biomass and primary productivity in open-ocean regions can be highly variable,
648   and biological impacts on carbonate chemistry are typically more pronounced in coastal or
649   upwelling systems (Duarte & Agusti, 1998; Williams & Follows, 2003). Moreover, the SNR
650   results indicate that in the North Atlantic, temperature-driven processes dominate short-term pH
651   variability, while the contribution of biological activity remains unclear due to overlapping
652   influences (see Table S1 in Supplementary Information). In the South Pacific, where all signals
653   fall below the noise threshold (SNR < 1; Table S2 in Supplementary Information), the observed
654   pH fluctuations may be driven by measurement uncertainty rather than a clear biological or
655   temperature-driven signal.
656

657   This variability further complicates assessments of air-sea CO_2 equilibration, as localized
658   biological conditions may transiently alter CO_2 dynamics, influencing the timescale for reaching
659   equilibrium. This is more obvious in the South Pacific, where some cycles display more
660   pronounced night-time stability (Fig. 5, Cycles 3, 6, 7 and 11), while others have noticeable day-
661   time fluctuations that could align with photosynthetic activity, which typically increase during
662   daylight hours (Fig. 5, Cycle 8; (Duarte & Agusti, 1998; Raven & Johnston, 1991). Cycle 8 in
663   the South Pacific shows a peak in observed pH around midday, likely due to increased
664   photosynthesis, followed by a decrease in the evening (Fig. 5). Other cycles do not show this
665   pattern as clearly (i.e., they even show a decrease of pH during the day), suggesting that, for
666   some cycles, respiration may dominate over photosynthesis also during daytime (Fig. 5). For
667   example, Cycle 9 displays significant variations in pH throughout the day, with notable
668   decreases during daylight hours (Fig. 5). Additionally, as some cycles appear to conform to

669 temperature-based pH expectations, the only minor deviations observed suggest biological
670 activity to be minor or represent a balanced biological system where photosynthesis and
671 respiration are in near-equilibrium (Fig. 5, Cycles 3 and 6).
672
673 Despite the strong impact of both abiotic and biotic factors on pH, some cycles exhibit fine-scale
674 trends that cannot be solely attributed to temperature fluctuations or biological activity. The fine-
675 scale trends observed, especially in Cycles 1 and 7 (Fig. 4), exceed what can be attributed to
676 temperature-induced changes alone and cannot be explained by biological activity, given the
677 atypically high carbon fixation rates required to explain the pH offsets (Basu & Mackey, 2018;
678 Wang et al., 2023). Indeed, the required biological carbon fixation would need to exceed 687 mg
679 C m^{-3} day^{-1} to explain the offset (Text S2). Typical rates in open ocean waters are much lower,
680 generally ranging from 50 to 150 mg C m^3 day^{-1} in nutrient-poor regions and can reach up to
681 1000 C m^{-3} day^{-1} in upwelling zones during phytoplankton blooms, which is not the case here
682 (Basu & Mackey, 2018; Wang et al., 2023).
683
684 Comparing the impact of biological activity based on the offsets between pH$_{temp}$ and pH$_{obs}$ with
685 chlorophyll-a fluorescence data also shows no clear pattern (Fig. S4 and S5). This is expected as
686 fluorescence does not necessarily reflect instantaneous photosynthetic activity. Instead,
687 fluorescence primarily indicates the presence and abundance of phytoplankton. Therefore, while
688 fluorescence can provide insights into the overall biomass of phytoplankton, it does not directly
689 correlate with photosynthesis and respiration. The absence of a clear correlation between
690 fluorescence and the daily pH cycle, with some cycles even showing a decrease in pH during
691 daytime, confirms that the influence of waters with distinct temperature-salinity properties
692 important in shaping the local high-resolution pH profiles.

693 **3.3 Variability and stability in spatio-temporal pH patterns**

694 As examined in Sect. 3.1, considerable spatial variability is observed in the North Atlantic (Fig.
695 8 and Fig. S8), and this heterogeneity introduces complexity in deciphering the relative
696 contributions of abiotic and biotic factors to pH fluctuations (Gruber & Sarmiento, 2002).
697 Residual plots for the North Atlantic suggest that the observed discrepancies between pH$_{obs}$ and
698 both pH$_{temp}$ and pH$_{temp,sal}$ are insignificant, indicating that variability in surface water
699 characteristics—which include but are not limited solely to temperature and salinity—do not
700 dominate the observed pH variability (Fig. 6 and 8; (Dumousseaud et al., 2010). The SNR results
701 further confirm that temperature-driven pH fluctuations are real signals in this region (SNR > 1;
702 Table S1 in Supplementary Information), supporting their role as key drivers of diel pH
703 variability. Therefore, the hourly fluctuations in pH$_{obs}$ and the observed discrepancies between
704 pH$_{obs}$ and pH$_{temp/sal}$ across various cycles in this ocean basin may not be attributed to pronounced
705 spatial variability (Fig. 4). The T/S diagram also demonstrates this spatial variability, showing a
706 wide range of pH values correlated with differing salinity and temperature profiles across waters
707 with distinct temperature-salinity properties (Fig. 8), reinforcing that spatial dynamics do not
708 significantly influence pH variation in this region. This is also supported by the relative stability
709 observed in Cycle 4, where the ship's consistent positioning (i.e. on station) highlights the role of
710 temporal variability rather than spatial variability (Fig. S6). Although water could still be moving
711 spatially around the ship, the variability could be due to some degree to different waters rather
712 than being limited to true in-situ temporal variability.
713

714 In contrast, the South Pacific cruise predominantly exhibits a stable transit through more
715 homogeneous surface waters as no SST gradient is observed, although it is not entirely free from
716 disruptions (Fig. 8 and Fig. S7; Qu and Lindstrom (2004). This suggests a limited role of
717 interactions between diverse surface waters. Despite the hourly fluctuations observed, all diel
718 cycles in the South Pacific tend to cluster closely around the mean pH for their respective 24-
719 hour periods, reflecting substantial stability within each cycle but considerable variability across
720 different days, particularly evident among consecutive cycles (Fig. 5). This underscores a clear
721 temporal delineation of diel cycles influenced by DIC changes (Fig. 5). However, the SNR
722 results indicate that all expected pH fluctuations in this region remain below the uncertainty
723 threshold (SNR < 1; Table S2 in Supplementary Information), making it difficult to determine
724 whether observed fluctuations reflect true environmental variability or are primarily within the
725 measurement uncertainty.

726 **3.4 Implications for air-sea CO_2 fluxes**

727 Our findings indicate that while temperature and salinity predominantly govern diel pH
728 fluctuations, additional variability arises from surface water dynamics and biological activity.
729 Temperature rapidly affects pH, but the slower rate of CO_2 equilibration with the atmosphere
730 moderates its impact on air-sea CO_2 fluxes. Although biological processes markedly influence
731 daily pH cycles, they do not fully account for the observed variability, especially in cases where
732 unusually high carbon fixation rates would be required to explain observed pH (Sect. 3.2).
733 Notably, the North Atlantic acted as a net sink of CO_2, whereas the South Pacific was a net
734 source to the atmosphere during the study period.

735

736 CO_2 fluxes were calculated for each complete diel cycle (Fig. 9). The flux calculations were
737 performed by computing the mean flux for each cycle from daily mean inputs (wind speed,
738 temperature, salinity, and $p$$CO_2$) and specifically for the hours 12 AM and 12 PM (LST) to
739 examine temporal variations within each cycle (Fig. 9). Despite different methods of calculation,
740 the CO_2 fluxes remained relatively consistent, indicating that the variations in pH and thus CO_2
741 flux do not significantly affect the air-sea CO_2 exchange in either basin.

742

743 This consistent result shows that, despite the processes influencing pH in these two ocean basins
744 during the study period, air-sea CO_2 exchange over longer timescales (e.g., months) can dampen
745 short-term pH variability, resulting in relatively low variability across short spatiotemporal scales
746 (kilometers/days).**4. Conclusions**

747 High-resolution pH data enabled by our novel optical measurement system provides valuable
748 insights into the complex and variable nature of surface ocean pH. Our observations in the North
749 Atlantic and South Pacific show that pH fluctuates on diel and hourly timescales, with variations
750 driven not only by temperature but also by the interplay between waters with distinct
751 temperature-salinity properties and biological activity. These factors do not operate in isolation,
752 making it difficult to attribute pH changes to a single dominant driver.Diel

753

754 diel
755 Although the processes governing pH variability are well-understood, our high-frequency
756 measurements demonstrate the challenge of disentangling their contributions at fine spatial and
757 temporal scales. This underscores the importance of continuous, high-frequency measurements,

758 which reveal the heterogeneity in surface pH that lower-resolution datasets might miss. In both
759 basins, the close correlation between pH_{TA,fCO_2} and observed pH across diel cycles suggests that
760 air-sea CO_2 exchange plays a key role in stabilizing pH despite temperature fluctuations. The
761 observed pH stability implies that the ship primarily encountered waters that had already
762 equilibrated with atmospheric CO_2, reinforcing the idea that temperature-driven pH changes
763 alone are not always sufficient to explain variability in surface ocean carbonate chemistry.
764
765
766 While our results indicate that fine-scale variability in these regions was relatively subtle—and
767 may not significantly impact large-scale assessments—this insight could only be gained through
768 high-resolution observations. This approach not only reveals the complexity of pH regulation but
769 also provides valuable insight into the fine-scale physical and biological interactions that shape
770 surface ocean chemistry. Importantly, although lower-resolution datasets may be sufficient for
771 capturing broad-scale patterns in surface ocean CO_2 chemistry, our findings highlight the critical
772 role of high-frequency measurements in refining regional understanding and improving
773 predictive models of ocean acidification and air-sea gas exchange.

774 *Data availability.* The hydrographic and biogeochemical data presented here, together with the
775 processing code is freely available online at https://github.com/louisedelaigue/NA-SP-HIGH-
776 RES-PH.

777 *Supplement.* The supplement related to this article is available online.

778 *Author contributions*. LD and MPH conceptualized the project. CG, AM, LQ, EPA, LD, MPH
779 and YO curated the data. LD, MPH and GJR performed the investigation. LD conceptualized the
780 methodology, used the necessary software, visualized the data and prepared the original draft of
781 the paper. LD, GJR, MPH, YO andCG reviewed and edited the paper.

782 *Competing interests.* The contact author has declared that neither they nor their co-authors have
783 any competing interests.

784 *Disclaimer.* Publisher's note: Copernicus Publications remains neutral with regard to
785 jurisdictional claims in published maps and institutional affiliations.

786 *Acknowledgements.* We are grateful to the officers and crew of the R/V *Sonne* and technical
787 support from GEOMAR for their support and assistance, and the opportunity to join cruises
788 SO279 and SO289. Special acknowledgment goes to Paul Battermann who greatly assisted in the
789 sampling aboard the FS Sonne during SO289. Funding for cruise SO289 came from the BMBF
790 (grant 03G0289NA) to EPA. We thank Karel Bakker and Sharyn Ossebaar for their help in the
791 lab – this work would not be possible without them. LD also wishes to thank Sorbonne
792 Université and the Institut de la mer de Villefranche (France), in particular the OMTAB team,
793 for hosting her during the later stage of this research project, as well as Jean-Pierre Gattuso,

794   Pierrick Lemasson and Elsa Simon for the many brainstorming sessions. Figure 2 schematic
795   made by cartographic design - faculty of Geosciences - Utrecht University.

796   **References**

797   Achterberg, E. P., Steiner, Z., & Galley, C. G. (2022). South Pacific GEOTRACES Cruise No.
798   SO289, 18 February 2022–08 April 2022, Valparaiso (Chile)–Noumea (New Caledonia),
799   GEOTRACES GP21.

800   Baines, S. B., Pace, M. L., & Karl, D. M. (1994). Why does the relationship between sinking
801   flux and planktonic primary production differ between lakes and oceans? *Limnology and*
802   *Oceanography*, *39*(2), 213-226.

803   Basu, S., & Mackey, K. R. M. (2018). Phytoplankton as Key Mediators of the Biological Carbon
804   Pump: Their Responses to a Changing Climate. *Sustainability*, *10*(3), 869.
805   https://www.mdpi.com/2071-1050/10/3/869

806   Beck, A., Borchert, E., Delaigue, L., Deng, F., Gueroun, S., Hamm, T., Jacob, O., Kaandorp, M.,
807   Kokuhennadige, H., & Kossel, E. (2021). NAPTRAM-Plastiktransportmechanismen,
808   Senken und Interaktionen mit Biota im Nordatlantik/NAPTRAM-North Atlantic plastic
809   transport mechanisms, sinks, and interactions with biota, Cruise No. SO279, Emden
810   (Germany)–Emden (Germany), 04.12. 2020–05.01. 2021.

811   Behrenfeld, M. J., & Falkowski, P. G. (1997). Photosynthetic rates derived from satellite-based
812   chlorophyll concentration. *Limnology and Oceanography*, *42*(1), 1-20.

813   Caldeira, K., & Wickett, M. E. (2005). Ocean model predictions of chemistry changes from
814   carbon dioxide emissions to the atmosphere and ocean. *Journal of Geophysical Research:*
815   *Oceans*, *110*(C9).

816   Chavez, F. P., Sevadjian, J., Wahl, C., Friederich, J., & Friederich, G. E. (2018). Measurements
817   of pCO2 and pH from an autonomous surface vehicle in a coastal upwelling system.
818   *Deep Sea Research Part II: Topical Studies in Oceanography*, *151*, 137-146.
819   https://doi.org/https://doi.org/10.1016/j.dsr2.2017.01.001

820   Cornwall, C. E., Hepburn, C. D., McGraw, C. M., Currie, K. I., Pilditch, C. A., Hunter, K. A.,
821   Boyd, P. W., & Hurd, C. L. (2013). Diurnal fluctuations in seawater pH influence the
822   response of a calcifying macroalga to ocean acidification. *Proceedings of the Royal*
823   *Society B: Biological Sciences*, *280*(1772), 20132201.
824   https://doi.org/doi:10.1098/rspb.2013.2201

825   Couldrey, M. P., Oliver, K. I., Yool, A., Halloran, P. R., & Achterberg, E. P. (2016). On which
826   timescales do gas transfer velocities control North Atlantic CO2 flux variability? *Global*
827   *Biogeochemical Cycles*, *30*(5), 787-802.

828   Cryer, S., Carvalho, F., Wood, T., Strong, J. A., Brown, P., Loucaides, S., Young, A., Sanders,
829   R., & Evans, C. (2020). Evaluating the Sensor-Equipped Autonomous Surface Vehicle C-
830   Worker 4 as a Tool for Identifying Coastal Ocean Acidification and Changes in
831   Carbonate Chemistry. *Journal of Marine Science and Engineering*, *8*(11), 939.
832   https://www.mdpi.com/2077-1312/8/11/939

833   Delaigue, L., Ourradi, Y., Bakker, K., Battermann, P., Galley, C., & Humphreys, M. P. (2023a).
834   *Discrete underway surface seawater dissolved inorganic carbon and total alkalinity for*
835   *R/V Sonne cruise SO289* (Version V2) NIOZ. https://doi.org/doi:10.25850/nioz/7b.b.vf

836   Delaigue, L., Ourradi, Y., Bakker, K., Battermann, P., Galley, C., & Humphreys, M. P. (2023b).
837   *Underway surface seawater high-resolution pH time series for R/V Sonne cruise SO289*
838   (Version V2) NIOZ. https://doi.org/doi:10.25850/nioz/7b.b.uf

839   Delaigue, L., Ourradi, Y., Ossebar, S., Battermann, P., Galley, C., & Humphreys, M. P. (2023).
840   *CTD seawater dissolved inorganic carbon and total alkalinity for R/V Sonne cruise*
841   *SO289* (Version V6) NIOZ. https://doi.org/doi:10.25850/nioz/7b.b.tf

842   Delaigue, L., van Ooijen, J., & Humphreys, M. P. (2021a). *CTD seawater dissolved inorganic*
843   *carbon, total alkalinity and nutrients for R/V Sonne cruise SO279* (Version V2) NIOZ.
844   https://doi.org/doi:10.25850/nioz/7b.b.kc

845   Delaigue, L., van Ooijen, J., & Humphreys, M. P. (2021b). *Discrete underway surface seawater*
846   *dissolved inorganic carbon, total alkalinity and nutrients for R/V Sonne cruise SO279*
847   (Version V2) NIOZ. https://doi.org/doi:10.25850/nioz/7b.b.lc

848   Delaigue, L., van Ooijen, J., & Humphreys, M. P. (2021c). *Underway surface seawater high-*
849   *resolution pH time series for R/V Sonne cruise SO279* (Version V2) NIOZ.
850   https://doi.org/doi:10.25850/nioz/7b.b.mc

851   DeVries, T. (2022). The Ocean Carbon Cycle. *Annual Review of Environment and Resources*,
852   *47*(1), 317-341. https://doi.org/10.1146/annurev-environ-120920-111307

853   Dickson, A., & Millero, F. J. (1987). A comparison of the equilibrium constants for the
854   dissociation of carbonic acid in seawater media. *Deep Sea Research Part A.*
855   *Oceanographic Research Papers*, *34*(10), 1733-1743.

856   Dickson, A. G. (1990). Standard potential of the reaction: $AgCl(s) + 12H_2(g) = Ag(s) + HCl(aq)$,
857   and and the standard acidity constant of the ion HSO_4^- in synthetic sea water from
858   273.15 to 318.15 K. *The Journal of Chemical Thermodynamics*, *22*(2), 113-127.
859   https://doi.org/https://doi.org/10.1016/0021-9614(90)90074-Z

860   Dickson, A. G., & Riley, J. P. (1979). The estimation of acid dissociation constants in sea-water
861   media from potentiometric titrations with strong base. II. The dissociation of phosphoric
862   acid. *Marine Chemistry*, *7*(2), 101-109. https://doi.org/https://doi.org/10.1016/0304-
863   4203(79)90002-1

864   Dickson, A. G., Sabine, C. L., & Christian, J. R. (2007). *Guide to best practices for ocean CO2*
865   *measurements*. North Pacific Marine Science Organization.

866   Doney, S. C., Busch, D. S., Cooley, S. R., & Kroeker, K. J. (2020). The Impacts of Ocean
867   Acidification on Marine Ecosystems and Reliant Human Communities. *Annual Review of*
868   *Environment and Resources*, *45*(Volume 45, 2020), 83-112.
869   https://doi.org/https://doi.org/10.1146/annurev-environ-012320-083019

870   Duarte, C. M., & Agusti, S. (1998). The CO2 balance of unproductive aquatic ecosystems.
871   *Science*, *281*(5374), 234-236. https://doi.org/10.1126/science.281.5374.234

872   Dumousseaud, C., Achterberg, E. P., Tyrrell, T., Charalampopoulou, A., Schuster, U., Hartman,
873   M., & Hydes, D. J. (2010). Contrasting effects of temperature and winter mixing on the
874   seasonal and inter-annual variability of the carbonate system in the Northeast Atlantic
875   Ocean. *Biogeosciences*, *7*(5), 1481-1492. https://doi.org/10.5194/bg-7-1481-2010

876   Egea, L. G., Jiménez-Ramos, R., Hernández, I., Bouma, T. J., & Brun, F. G. (2018). Effects of
877   ocean acidification and hydrodynamic conditions on carbon metabolism and dissolved
878   organic carbon (DOC) fluxes in seagrass populations. *PLOS ONE*, *13*(2), e0192402.
879   https://doi.org/10.1371/journal.pone.0192402

880   Egilsdottir, H., Noisette, F., Noël, L. M. L. J., Olafsson, J., & Martin, S. (2013). Effects of pCO2
881   on physiology and skeletal mineralogy in a tidal pool coralline alga Corallina elongata.
882   *Marine Biology*, *160*(8), 2103-2112. https://doi.org/10.1007/s00227-012-2090-7

883   Egleston, E. S., Sabine, C. L., & Morel, F. M. (2010). Revelle revisited: Buffer factors that
884   quantify the response of ocean chemistry to changes in DIC and alkalinity. *Global
885   Biogeochemical Cycles*, *24*(1).
886   Emerson, S., & Hedges, J. (2008). *Chemical oceanography and the marine carbon cycle*.
887   Cambridge University Press.
888   Faassen, K. A. P., Nguyen, L. N. T., Broekema, E. R., Kers, B. A. M., Mammarella, I., Vesala,
889   T., Pickers, P. A., Manning, A. C., Vilà-Guerau de Arellano, J., Meijer, H. A. J., Peters,
890   W., & Luijkx, I. T. (2023). Diurnal variability of atmospheric O2, CO2, and their
891   exchange ratio above a boreal forest in southern Finland. *Atmos. Chem. Phys.*, *23*(2),
892   851-876. https://doi.org/10.5194/acp-23-851-2023
893   Falkowski, P. G. (1994). The role of phytoplankton photosynthesis in global biogeochemical
894   cycles. *Photosynthesis Research*, *39*(3), 235-258. https://doi.org/10.1007/BF00014586
895   Falkowski, P. G., & Raven, J. A. (2013). *Aquatic photosynthesis*. Princeton University Press.
896   Fay, A. R., Gregor, L., Landschützer, P., McKinley, G. A., Gruber, N., Gehlen, M., Iida, Y.,
897   Laruelle, G. G., Rödenbeck, C., Roobaert, A., & Zeng, J. (2021). SeaFlux: harmonization
898   of air–sea CO2 fluxes from surface pCO2 data products using a standardized approach.
899   *Earth Syst. Sci. Data*, *13*(10), 4693-4710. https://doi.org/10.5194/essd-13-4693-2021
900   Fietzek, P., Fiedler, B., Steinhoff, T., & Körtzinger, A. (2014). In situ quality assessment of a
901   novel underwater p CO 2 sensor based on membrane equilibration and NDIR
902   spectrometry. *Journal of Atmospheric and Oceanic Technology*, *31*(1), 181-196.
903   Figuerola, B., Hancock, A. M., Bax, N., Cummings, V. J., Downey, R., Griffiths, H. J., Smith, J.,
904   & Stark, J. S. (2021). A Review and Meta-Analysis of Potential Impacts of Ocean
905   Acidification on Marine Calcifiers From the Southern Ocean [Review]. *Frontiers in
906   Marine Science*, *8*. https://doi.org/10.3389/fmars.2021.584445
907   Frankignoulle, M. (1994). A complete set of buffer factors for acid/base CO2 system in seawater.
908   *Journal of Marine Systems*, *5*(2), 111-118.
909   Fritsch, F. N., & Carlson, R. E. (1980). Monotone Piecewise Cubic Interpolation. *SIAM Journal
910   on Numerical Analysis*, *17*(2), 238-246. https://doi.org/10.1137/0717021
911   Fujii, M., Takao, S., Yamaka, T., Akamatsu, T., Fujita, Y., Wakita, M., Yamamoto, A., & Ono,
912   T. (2021). Continuous Monitoring and Future Projection of Ocean Warming,
913   Acidification, and Deoxygenation on the Subarctic Coast of Hokkaido, Japan [Original
914   Research]. *Frontiers in Marine Science*, *8*. https://doi.org/10.3389/fmars.2021.590020
915   Gattuso, J.-P., Magnan, A., Billé, R., Cheung, W. W., Howes, E. L., Joos, F., Allemand, D.,
916   Bopp, L., Cooley, S. R., & Eakin, C. M. (2015). Contrasting futures for ocean and society
917   from different anthropogenic CO2 emissions scenarios. *Science*, *349*(6243), aac4722.
918   Gruber, N., & Sarmiento, J. L. (2002). Large-scale biogeochemical-physical interactions in
919   elemental cycles. *The Sea*, *12*, 337-399.
920   Ho, D. T., Law, C. S., Smith, M. J., Schlosser, P., Harvey, M., & Hill, P. (2006). Measurements
921   of air-sea gas exchange at high wind speeds in the Southern Ocean: Implications for
922   global parameterizations. *Geophysical Research Letters*, *33*(16).
923   Hofmann, G. E., Smith, J. E., Johnson, K. S., Send, U., Levin, L. A., Micheli, F., Paytan, A.,
924   Price, N. N., Peterson, B., Takeshita, Y., Matson, P. G., Crook, E. D., Kroeker, K. J.,
925   Gambi, M. C., Rivest, E. B., Frieder, C. A., Yu, P. C., & Martz, T. R. (2011). High-
926   Frequency Dynamics of Ocean pH: A Multi-Ecosystem Comparison. *PLOS ONE*, *6*(12),
927   e28983. https://doi.org/10.1371/journal.pone.0028983

Humphreys, M. P., Lewis, E. R., Sharp, J. D., & Pierrot, D. (2022). PyCO2SYS v1.8: marine carbonate system calculations in Python. *Geosci. Model Dev.*, *15*(1), 15-43. https://doi.org/10.5194/gmd-15-15-2022

James, R. K., van Katwijk, M. M., van Tussenbroek, B. I., van der Heide, T., Dijkstra, H. A., van Westen, R. M., Pietrzak, J. D., Candy, A. S., Klees, R., Riva, R. E. M., Slobbe, C. D., Katsman, C. A., Herman, P. M. J., & Bouma, T. J. (2020). Water motion and vegetation control the pH dynamics in seagrass-dominated bays. *Limnology and Oceanography*, *65*(2), 349-362. https://doi.org/https://doi.org/10.1002/lno.11303

Jiang, L.-Q., Carter, B. R., Feely, R. A., Lauvset, S. K., & Olsen, A. (2019). Surface ocean pH and buffer capacity: past, present and future. *Scientific reports*, *9*(1), 1-11.

Johnson, K. S., Riser, S. C., & Karl, D. M. (2010). Nitrate supply from deep to near-surface waters of the North Pacific subtropical gyre. *Nature*, *465*(7301), 1062-1065.

Jokiel, P. L., Jury, C. P., & Rodgers, K. S. (2014). Coral-algae metabolism and diurnal changes in the CO2-carbonate system of bulk sea water. *PeerJ*, *2*, e378. https://doi.org/10.7717/peerj.378

Jones, D. C., Ito, T., Takano, Y., & Hsu, W. C. (2014). Spatial and seasonal variability of the air-sea equilibration timescale of carbon dioxide. *Global Biogeochemical Cycles*, *28*(11), 1163-1178.

Lee, K., Tong, L. T., Millero, F. J., Sabine, C. L., Dickson, A. G., Goyet, C., Park, G. H., Wanninkhof, R., Feely, R. A., & Key, R. M. (2006). Global relationships of total alkalinity with salinity and temperature in surface waters of the world's oceans. *Geophysical Research Letters*, *33*(19).

Li, A., Aubeneau, A. F., King, T., Cory, R. M., Neilson, B. T., Bolster, D., & Packman, A. I. (2019). Effects of vertical hydrodynamic mixing on photomineralization of dissolved organic carbon in arctic surface waters. *Environmental Science: Processes & Impacts*, *21*(4), 748-760.

Liu, X., Patsavas, M. C., & Byrne, R. H. (2011). Purification and characterization of meta-cresol purple for spectrophotometric seawater pH measurements. *Environmental Science & Technology*, *45*(11), 4862-4868.

Longhurst, A. R. (2010). *Ecological geography of the sea*. Elsevier.

Lueker, T. J., Dickson, A. G., & Keeling, C. D. (2000). Ocean pCO2 calculated from dissolved inorganic carbon, alkalinity, and equations for K1 and K2: validation based on laboratory measurements of CO2 in gas and seawater at equilibrium. *Marine Chemistry*, *70*(1-3), 105-119.

Martz, T. R., Connery, J. G., & Johnson, K. S. (2010). Testing the Honeywell Durafet® for seawater pH applications. *Limnology and Oceanography: Methods*, *8*(5), 172-184. https://doi.org/https://doi.org/10.4319/lom.2010.8.172

Middelburg, J. J., Soetaert, K., & Hagens, M. (2020). Ocean Alkalinity, Buffering and Biogeochemical Processes. *Reviews of Geophysics*, *58*(3), e2019RG000681. https://doi.org/10.1029/2019rg000681

Millero, F. J. (2007). The marine inorganic carbon cycle. *Chemical reviews*, *107*(2), 308-341.

Millero, F. J., & Poisson, A. (1981). International one-atmosphere equation of state of seawater. *Deep Sea Research Part A. Oceanographic Research Papers*, *28*(6), 625-629.

Orr, J. C., Fabry, V. J., Aumont, O., Bopp, L., Doney, S. C., Feely, R. A., Gnanadesikan, A., Gruber, N., Ishida, A., Joos, F., Key, R. M., Lindsay, K., Maier-Reimer, E., Matear, R., Monfray, P., Mouchet, A., Najjar, R. G., Plattner, G.-K., Rodgers, K. B.,…Yool, A.

(2005). Anthropogenic ocean acidification over the twenty-first century and its impact on calcifying organisms. *Nature*, *437*(7059), 681-686. https://doi.org/10.1038/nature04095

Osborne, E. B., Thunell, R. C., Gruber, N., Feely, R. A., & Benitez-Nelson, C. R. (2020). Decadal variability in twentieth-century ocean acidification in the California Current Ecosystem. *Nature Geoscience*, *13*(1), 43-49. https://doi.org/10.1038/s41561-019-0499-z

Possenti, L., Humphreys, M. P., Bakker, D. C. E., Cobas-García, M., Fernand, L., Lee, G. A., Pallottino, F., Loucaides, S., Mowlem, M. C., & Kaiser, J. (2021). Air-Sea Gas Fluxes and Remineralization From a Novel Combination of pH and O2 Sensors on a Glider [Original Research]. *Frontiers in Marine Science*, *8*(1210). https://doi.org/10.3389/fmars.2021.696772

Price, N. N., Martz, T. R., Brainard, R. E., & Smith, J. E. (2012). Diel Variability in Seawater pH Relates to Calcification and Benthic Community Structure on Coral Reefs. *PLOS ONE*, *7*(8), e43843. https://doi.org/10.1371/journal.pone.0043843

Qu, L., Xu, J., Sun, J., Li, X., & Gao, K. (2017). Diurnal pH fluctuations of seawater influence the responses of an economic red macroalga Gracilaria lemaneiformis to future CO2-induced seawater acidification. *Aquaculture*, *473*, 383-388. https://doi.org/https://doi.org/10.1016/j.aquaculture.2017.03.001

Qu, T., & Lindstrom, E. J. (2004). Northward intrusion of Antarctic Intermediate Water in the western Pacific. *Journal of Physical Oceanography*, *34*(9), 2104-2118.

Raven, J. A., & Johnston, A. M. (1991). Mechanisms of inorganic-carbon acquisition in marine phytoplankton and their implications for the use of other resources. *Limnology and Oceanography*, *36*(8), 1701-1714.

Richardson, D. J. (2000). Bacterial respiration: a flexible process for a changing environment. *Microbiology*, *146*(3), 551-571.

Staudinger, C., Strobl, M., Breininger, J., Klimant, I., & Borisov, S. M. (2019). Fast and stable optical pH sensor materials for oceanographic applications. *Sensors and Actuators B: Chemical*, *282*, 204-217. https://doi.org/https://doi.org/10.1016/j.snb.2018.11.048

Staudinger, C., Strobl, M., Fischer, J. P., Thar, R., Mayr, T., Aigner, D., Müller, B. J., Müller, B., Lehner, P., Mistlberger, G., Fritzsche, E., Ehgartner, J., Zach, P. W., Clarke, J. S., Geißler, F., Mutzberg, A., Müller, J. D., Achterberg, E. P., Borisov, S. M., & Klimant, I. (2018). A versatile optode system for oxygen, carbon dioxide, and pH measurements in seawater with integrated battery and logger. *Limnology and Oceanography: Methods*, *16*(7), 459-473. https://doi.org/https://doi.org/10.1002/lom3.10260

Stoll, M., Bakker, K., Nobbe, G., & Haese, R. (2001). Continuous-flow analysis of dissolved inorganic carbon content in seawater. *Analytical Chemistry*, *73*(17), 4111-4116.

Strickland, J. D. H., & Parsons, T. R. (1972). A practical handbook of seawater analysis.

Stumm, W., & Morgan, J. J. (2012). *Aquatic chemistry: chemical equilibria and rates in natural waters*. John Wiley & Sons.

Sutton, A. J., Feely, R. A., Maenner-Jones, S., Musielwicz, S., Osborne, J., Dietrich, C., Monacci, N., Cross, J., Bott, R., Kozyr, A., Andersson, A. J., Bates, N. R., Cai, W. J., Cronin, M. F., De Carlo, E. H., Hales, B., Howden, S. D., Lee, C. M., Manzello, D. P.,…Weller, R. A. (2019). Autonomous seawater pCO2 and pH time series from 40 surface buoys and the emergence of anthropogenic trends. *Earth Syst. Sci. Data*, *11*(1), 421-439. https://doi.org/10.5194/essd-11-421-2019

1018 Takahashi, T., Sutherland, S. C., Feely, R. A., & Wanninkhof, R. (2006). Decadal change of the
1019   surface water pCO2 in the North Pacific: A synthesis of 35 years of observations. *Journal*
1020   *of Geophysical Research: Oceans*, *111*(C7).
1021 Tilstone, G. H., Figueiras, F., Lorenzo, L. M., & Arbones, B. (2003). Phytoplankton
1022   composition, photosynthesis and primary production during different hydrographic
1023   conditions at the Northwest Iberian upwelling system. *Marine Ecology Progress Series*,
1024   *252*, 89-104.
1025 Uppström, L. R. (1974). The boron/chlorinity ratio of deep-sea water from the Pacific Ocean.
1026   *Deep Sea Research and Oceanographic Abstracts*, *21*(2), 161-162.
1027   https://doi.org/https://doi.org/10.1016/0011-7471(74)90074-6
1028 Vallis, G. K. (2017). *Atmospheric and oceanic fluid dynamics*. Cambridge University Press.
1029 Wang, X., Yin, Z., Chen, J., & Liu, J. (2023). Phytoplankton Carbon Utilization Strategies and
1030   Effects on Carbon Fixation. *Water*, *15*(11), 2137. https://www.mdpi.com/2073-
1031   4441/15/11/2137
1032 Wei, Z., Zhang, Y., Yang, F., & Long, L. (2022). Diurnal fluctuations in seawater pCO2 amplify
1033   the negative effects of ocean acidification on the biotic performance of the calcifying
1034   macroalga Halimeda opuntia [Original Research]. *Frontiers in Marine Science*, *9*.
1035   https://doi.org/10.3389/fmars.2022.968740
1036 Williams, R. G., & Follows, M. J. (2003). Physical transport of nutrients and the maintenance of
1037   biological production. In *Ocean biogeochemistry: The role of the ocean carbon cycle in*
1038   *global change* (pp. 19-51). Springer.
1039 Wu, Y., Hain, M. P., Humphreys, M. P., Hartman, S., & Tyrrell, T. (2019). What drives the
1040   latitudinal gradient in open-ocean surface dissolved inorganic carbon concentration?
1041   *Biogeosciences*, *16*(13), 2661-2681. https://doi.org/10.5194/bg-16-2661-2019
1042 Zeebe, R. E., & Wolf-Gladrow, D. A. (2001). *CO2 in seawater: equilibrium, kinetics, isotopes*.
1043   http://site.ebrary.com/id/10190754
1044 Zehr, J. P., & Kudela, R. M. (2011). Nitrogen cycle of the open ocean: from genes to
1045   ecosystems. *Annual Review of Marine Science*, *3*, 197-225.
1046
1047